

Reconciling the bottom-up and top-down estimates of the methane chemical sink using multiple observations

Yuanhong Zhao^{1,2,3}, Marielle Saunois³, Philippe Bousquet³, Xin Lin³, Michaela I. Hegglin^{4, 5}, Josep G. Canadell⁶, Robert B. Jackson⁷, and Bo Zheng⁸

5

¹ Frontier Science Center for Deep Ocean Multispheres and Earth System (FDOMES) and Physical Oceanography Laboratory, Ocean University of China, Qingdao, China

² College of Oceanic and Atmospheric Sciences, Ocean University of China, Qingdao, China

³ Laboratoire des Sciences du Climat et de l'Environnement, LSCE-IPSL (CEA-CNRS-UVSQ),
10 Université Paris-Saclay, 91191 Gif-sur-Yvette, France

⁴ Institute of Energy and Climate Research – Stratosphere (IEK-7), Forschungszentrum Jülich GmbH,
52425 Jülich, Germany

⁵ Department of Meteorology, University of Reading, Earley Gate, Reading RG6 6BB, United Kingdom

⁶ Global Carbon Project, CSIRO Oceans and Atmosphere, Canberra, Australian Capital Territory 2601,
15 Australia

⁷ Earth System Science Department, Woods Institute for the Environment, and Precourt Institute for
Energy, Stanford University, Stanford, CA 94305, USA

⁸ Institute of Environment and Ecology, Tsinghua Shenzhen International Graduate School, Tsinghua
20 University, Shenzhen 518055, China

Correspondence to: Yuanhong Zhao (zhaoyuanhong@ouc.edu.cn)

25

30

35 **Abstract**

The methane chemical sink estimated by atmospheric chemistry models (bottom-up method) is significantly larger than estimates based on methyl-chloroform (MCF) inversions (top-down method). The difference is partly attributable to large uncertainties in hydroxyl radical (OH) concentrations simulated by the atmospheric chemistry models used to derive the bottom-up estimates. In this study, we propose a new approach based on OH precursor observations and a chemical box model. This approach contributes to improving the 3-dimensional distributions of tropospheric OH radicals obtained from atmospheric chemistry models and reconciling bottom-up and top-down estimates of the chemical loss of atmospheric methane. By constraining simulated OH precursors with observations, the global tropospheric column-averaged air-mass-weighted OH concentration ($[\text{OH}]_{\text{trop-M}}$) is $\sim 10 \times 10^5 \text{ molec cm}^{-3}$ (which is $2 \times 10^5 \text{ molec cm}^{-3}$ lower than the original model-simulated global $[\text{OH}]_{\text{trop-M}}$) and agrees with that obtained by the top-down method based on MCF inversions. With OH constrained by precursor observations, the methane chemical loss is 471-508 Tg yr^{-1} , averaged from 2000 to 2009. The new adjusted estimate is in the range of the latest top-down estimate of the Global Carbon Project (GCP) (459-516 Tg yr^{-1}) contrary to the bottom-up estimates using the original model-simulated OH fields (577-612 Tg yr^{-1}). The overestimation of global $[\text{OH}]_{\text{trop-M}}$ and methane chemical loss simulated by the atmospheric chemistry models is caused primarily by the models' underestimation of carbon monoxide and total ozone column, and overestimation of nitrogen dioxide. Our results highlight that constraining the model simulated OH fields with available OH precursor observations can help improve bottom-up estimates of the global methane sink.

55

60

Introduction

Methane (CH₄) is a potent greenhouse gas, with its 100-year global warming potential 27 (for non-fossil CH₄) and 30 times (for fossil CH₄) times that of CO₂ (Forster et al., 2021). The tropospheric CH₄ mixing ratios have increased by more than 1.6 times between pre-industrial and the present day, resulting in 0.54 ±0.11 W m⁻² radiative forcing from 1750 to 2019 (Forster et al., 2021). After a short-term stabilization during 2000-2006, the atmospheric methane mixing ratio rose increasingly quickly from 5 ppbv yr⁻¹ in 2006 to 17 ppbv yr⁻¹ in 2021 based on surface networks (Dlugokencky, NOAA/GML,2022). The rapid growth in atmospheric CH₄ over the recent decade further challenges meeting the 1.5-2.0°C targets of the Paris Agreement (Nisbet et al., 2019) and therefore is becoming an increasing concern (Jackson et al. 2020).

Understanding the drivers of atmospheric methane changes rely on accurate estimates of the global methane budget, as methane concentrations in the atmosphere are the net balance between emissions and sinks. To estimate this budget, the Global Carbon Project (GCP) has established the global CH₄ budget by gathering up-to-date observations and model information (Kirschke et al. 2013; Saunio et al., 2016; 2017; 2020). One of the remaining largest uncertainties, as pointed out by the most recent CH₄ budget (Saunio et al., 2020), is the chemical loss of CH₄. The chemical loss of CH₄ stems mainly through the reaction of CH₄ with hydroxyl radical (OH), which is also the most important CH₄ sink.

The hydroxyl radical (OH) is a key species in tropospheric chemistry that reacts with most greenhouse gases and air pollutants (Levy, 1971), being the main oxidant of the lower atmosphere. Due to its extremely short lifetime (typically 1 second) and spatial variability, direct observations do not allow for the quantification of the global [OH] distributions. The [OH] for calculating the chemical sink of CH₄ is thus estimated either from top-down or bottom-up methods. The top-down method estimates [OH] mainly

85 through inversions constrained by independent observations of 1-1-1trichloroethane (methyl chloroform, MCF), assuming that emissions of this compound are well known. Such MCF-based top-down methods have been widely used in the scientific community to derive OH trends but it can only yield the global to latitudinal mean [OH] due to the sparse MCF observations and does not represent the chemical feedback on OH (e.g., Prinn et al., 2001; Bousquet et al., 2005; Montzka et al., 2011; Naus et al., 2021; Patra et al., 90 2020). Bottom-up approaches on the other hand simulate the [OH] by atmospheric chemistry models to account for the chemical mechanisms that determine OH production and loss, but their estimates of the global mean [OH] usually disagree with MCF-based estimates (Naik et al., 2013; Zhao et al., 2019).

The global [OH] estimated by bottom-up model-based and top-down MCF-based methods are different 95 in magnitudes, inter-annual variations, and trends, resulting in large differences in estimated CH₄ sinks between the two methods. In the last global CH₄ budget, most of the OH fields used to estimate the bottom-up CH₄ sink were obtained from the atmospheric chemistry models that participated in the IGAC/SPARC Chemistry-Climate Model Initiative Phase-1 (CCMI-1) project. However, these models showed a wide range of $9.4\text{-}14.4 \times 10^5$ molec cm⁻³ in mean tropospheric column-averaged airmass- 100 weighted [OH] ([OH]_{trop-M}) (Zhao et al., 2019; Saunois et al., 2020), thus mostly higher than the values estimated by the MCF-based inversions ($\sim 10 \times 10^5$ molec cm⁻³; Prinn et al., 2001; Bousquet et al., 2005). Indeed, the mean CH₄ chemical loss for 2000-2009, as calculated by bottom-up approaches, is 595 Tg yr⁻¹ (range 489-749 Tg yr⁻¹), much higher than the 505 Tg yr⁻¹ (range 459-516 Tg yr⁻¹) estimated by top-down CH₄ inversions (Saunois et al., 2020). Those top-down inversions using box models indicate that 105 the [OH] changes may have influenced recent CH₄ trends, although with large uncertainties (Turner et al., 2017; Rigby et al., 2017) while more recent 3D inversions show no significant trend in [OH] after 2000 (Naus et al., 2021; Patra et al., 2021). In contrast to top-down MCF-based inversions, atmospheric chemistry models simulate a positive decadal trend in [OH] and consequently CH₄ chemical loss from

the 1980s (Zhao et al., 2020b).

110

Reconciling the bottom-up and top-down estimates of the methane chemical sink is essential for a more accurate estimate of the global methane budget and to better attribute the observed changes in atmospheric growth rates of CH₄. One way to improve the bottom-up estimates of the CH₄ sink and thus reconcile the difference is to correct the [OH] simulated by atmospheric models using observations of OH precursors.

115

Indeed, uncertainties in the [OH] simulated by atmospheric models can be attributed to biases in precursor concentrations. For example, Naik et al. (2013) found that an underestimation of carbon monoxide (CO) in the Northern Hemisphere can contribute to the overestimation of [OH] in this hemisphere; Strode et al. (2015) estimated that removing the model bias in O₃ and water vapor (H₂O_(g)) and reducing northern hemispheric nitrogen oxides (NO_x=NO+NO₂) emissions can reduce a high bias in the global tropospheric OH burden by 10%; Nicely et al. (2017; 2020) found that the inter-model difference in tropospheric [OH] is mainly driven by the difference in model simulated ultraviolet light flux to the troposphere, the tropospheric O₃, CO, and NO_x mixing ratio. In addition, the budget analysis of OH production and loss showed that about 90% of OH production is directly related to stratospheric and tropospheric ozone (O₃), H₂O_(g), and nitrogen oxide (NO), and ~60% of OH is removed by reaction with CO, CH₄ and formaldehyde (CH₂O) (Lelieveld et al., 2016; Zhao et al., 2020b). Thus, bottom-up estimates of the CH₄ sink from chemistry transport models can be improved if one can reduce the biases due to these OH precursors in modeled [OH].

120

125

130

Fortunately, several satellites have collected long-term continuous observations of the aforementioned OH precursors with global coverage, providing the opportunity to evaluate and improve bottom-up estimates of the CH₄ sink. The chemistry reanalysis that assimilates satellite observations of O₃, CO, NO₂, nitric acid (HNO₃), and CO shows significant improvement on both global OH burden and inter-

hemispheric gradient (Miyazaki et al., 2020). Such data assimilation methods can well balance the model and observation uncertainties, but they are not easy to apply to different models that simulate the broad range of global OH burden (Naik et al., 2013; Zhao et al., 2019). In addition, they do not allow partitioning the OH bias due to each precursor. In this context, the main objective of this study is to explore a simple approach to reconcile bottom-up and top-down estimates of the CH₄ sink by (i) improving the simulated atmospheric OH fields using multiple satellite observations and meteorological data from reanalysis and (ii) assessing the contribution of each main OH precursor to the bias in simulated [OH] and CH₄ sink. As a result, top-down estimates of CH₄ emissions will also benefit from the improved 3D distributions of [OH] (Zhao et al., 2020a; Saunio et al. 2020). We first evaluate the OH precursors (CO, CH₄, O₃, CH₂O, and NO₂, the total column O₃, and H₂O_(g)) simulated for the year 2010 by the CESM1-CAM4chem and GEOSCCM; these models participated in the CCMI-1 project and were used to estimate the global methane sink in Saunio et al. (2020) and represent two different chemical mechanisms. We then estimate the observation-based OH fields by correcting model biases of the two modeled OH fields due to the above-mentioned OH precursors using the Dynamically Simple Model of Atmospheric Chemical Complexity (DSMACC). By doing so, we quantify the bias in tropospheric [OH] attributable to each precursor. Finally, we estimate the chemical sink of CH₄ using the observation-based OH field and, based on the uncertainties inferred for [OH], we reveal the dominant factors contributing to the uncertainties in CH₄ chemical sink at the global and regional scales.

2 Method

2.1 Observational data

The total column O₃, which mainly influences the O (¹D) photolysis rate, is constrained by the National Aeronautics and Space Administration (NASA) Solar Backscatter Ultraviolet (SBUV) Merged Ozone Data Set (MOD) (Frith et al., 2014). The SBUV/MOD column O₃ data are derived by combining

observations from nine SBUV-type instruments aboard the NASA Aura satellite. The monthly O₃ columns are available 5° zonal mean.

160 Tropospheric O₃ is important in determining OH production. We constrain its spatial distributions using the tropospheric column O₃ data from the combined Aura Ozone Monitoring Instrument/Microwave Limb Sounder (OMI/MLS) satellite observations, which are generated by subtracting the co-located MLS limb measurements (integrated over the stratosphere to derive stratospheric column ozone) from total column ozone retrieved by OMI, an Ultraviolet/Visible nadir solar backscatter spectrometer (Ziemke et al., 2006).

165 The tropospheric nitrogen oxide family (NO_x=NO+NO₂) participates in both OH production (reaction of nitrogen oxide (NO) with hydroperoxyl radical (HO₂) or organic peroxy radicals (RO₂)) and loss (mainly reaction of NO₂ with OH). In the Dynamically Simple Model of Atmospheric Chemical Complexity (DSMACC) used in this study (see section 2.3), the total reactive nitrogen (NO_y) is constrained by either
170 NO₂ or NO concentrations. We constrain the spatial distributions of the boundary layer NO_y using satellite observations of NO₂ tropospheric vertical column density (VCD) of the Quality Assurance for Essential Climate Variables (QA4ECV) OMI NO₂ retrieval product (Boersma et al., 2018). Due to its short lifetime, NO_x emitted from the surface mainly remains within the planetary boundary layer. Thus, satellite-retrieved vertical column densities are widely used in understanding the NO₂ distributions within the
175 boundary layer instead of the whole troposphere (e.g., Cooper et al., 2020; Geddes et al., 2017).

We also constrain tropospheric CO, CH₄, and CH₂O to better represent OH loss in the troposphere. Distributions of CO and CH₂O are taken from 4D variational data assimilation of tropospheric CO column retrieved from the spaceborne Measurements Of Pollution In The Troposphere instrument v7 TIR-NIR
180 product (MOPITT v7, Deeter et al., 2017) and column CH₂O from OMI version3 product (González Abad

et al. 2015), respectively (Zheng et al., 2019). CH₄ distributions are taken from data assimilation of surface CH₄ observations (Zhao et al., 2020a) mainly from the U.S. National Oceanic and Atmospheric Administration (NOAA/ESRL, Dlugokencky et al., 1994). The assimilated surface CO concentration and CH₄ profiles show good agreement with independent ground-based observations and aircraft observations, respectively (Zheng et al., 2019; Zhao et al., 2020a).

Meteorological conditions, mainly water vapor (H₂O_(g)) and air temperature (T_a) can also influence tropospheric [OH]. The H₂O_(g) (represented as specific humidity) and T_a are constrained by the second Modern-Era Retrospective analysis for Research and Applications (MERRA-2) reanalysis data from NASA's Global Modeling and Assimilation Office (GMAO) (Gelaro et al. 2017).

2.2 The 3D atmospheric chemistry model simulations

The 3D distributions of monthly mean OH fields and OH precursors for the year 2010 are taken from the REF-C1 experiment of the IGAC/SPARC Chemistry-Climate Model Initiative Phase-1 (CCMI-1) (Hegglin and Lamarque, 2015; Morgenstern et al., 2017). The REF-C1 experiment is driven by state-of-the-art historical forcings and sea surface temperatures from observations and covers 51 years (1960-2010).

We include simulations from two models with different chemical mechanisms: (1) the Community Earth System Model (CESM) using the Community Atmosphere Model version 4 as atmosphere component (CESM1 CAM4-chem, Tilmes et al., 2015; 2016) and (2) the GEOS-5 Chemistry Climate Model (GEOSCCM; Molod et al., 2012, 2015; Oman et al., 2011, 2013; Nielsen et al., 2017). The tropospheric chemistry of CESM1 CAM4-chem is based on MOZART-4 mechanisms with minor updates (Emmons et al., 2010; Lamarque et al., 2012) and the GEOSCCM is based on the Global Modeling Initiative (GMI)

205 chemistry and transport model (Duncan et al., 2017), which was originally developed for the GEOS-
Chem model. The CO, NO₂, O₃, CH₄, CH₂O mixing ratios, total columns O₃, and metrological conditions
including T_a and H₂O_(g) simulated by CESM1 CAM4-chem and GEOSCCM in 2010 are compared with
the observational data described in Section 2.1 in the supplementary (Fig. S1, S2, and S3). We chose the
CESM1 CAM4-Chem and GEOSCCM in this study since (1) their global mean OH concentrations and
210 OH distributions (both horizontal and vertical) are around the multi-model mean values given by Zhao et
al. (2019), albeit not at the extreme of the model distribution; (2) the two models include multiple primary
non-methane volatile organic compounds (NMVOC) emissions (Morgenstern et al., 2017); (3) the
chemical box model DSMACC already include the MOZART-4 and GEOS-Chem chemical mechanisms
(section 2.3), which are similar to that used in CESM1 CAM4-Chem and GEOSCCM, respectively.

215

A detailed description of the two model settings related to OH and the CCMI-1 model experiments can
be found in Morgenstern et al. (2017) and Zhao et al. (2019).

2.3 The chemical box model DSMACC

220 Differing from 3D atmospheric chemistry models, which simulate the [OH] by gridded emissions
inventories of its precursors, a chemical box model simulates [OH] by prescribing precursor
concentrations and the meteorological states. Thus, one can estimate the sensitivity of [OH] to different
precursor concentrations and meteorological parameters. Here we use the Dynamically Simple Model of
Atmospheric Chemical Complexity (DSMACC; Emmerson and Evans, 2009) to estimate the sensitivity
225 of [OH] to chemical species including CO, NO₂, O₃, CH₄, CH₂O, the total column O₃, and meteorological
conditions including T_a and H₂O_(g) following the approach of Nicely et al. (2018).

The DSMACC model takes advantage of the chemical pre-processor (KPP) to generate the FORTRAN

code for a chosen chemical mechanism. In this study, the DSMACC model is compiled with MOZART-
230 4 and GEOS-Chem chemical mechanisms, respectively, to be consistent with the associated 3D models
CESM1 CAM4-chem and GEOSCCM. The clear-sky photolysis rates of chemical species are estimated
by the tropospheric ultraviolet and visible (TUV) radiation model. Forced by meteorological variables
($\text{H}_2\text{O}_{(\text{g})}$, T_{a} , and pressure), total column O_3 , and gas concentrations simulated by the CESM1 CAM4-chem
and GEOSCCM or generated from observations, and the diurnal cycle of the photolysis rates estimated
235 by TUV radiation model, the DSMACC is run forward until reaching the diurnal steady state of OH.
Nicely et al. (2018) have estimated the response of [OH] to changes in OH precursors by conducting
DSMACC model simulations for broad latitude and pressure bins. The results show that the $\text{H}_2\text{O}_{(\text{g})}$, NO_x ,
total column O_3 , and tropical expansion can lead to a positive trend in tropospheric [OH], offsetting most
of the negative trend led by the rising CH_4 concentrations from 1980 to 2015. Here for each month, we
240 run the DSMACC model for each model pixel of the 3D grid to better represent the heterogeneous spatial
distributions of OH. For example, the CESM1 CAM4-chem has 144 (longitude) \times 96 (latitudes) \times 13
(pressure level) model grids in the troposphere. For each sensitivity experiment (Sect. 2.4), we therefore
conduct 179,712 DSMACC model simulations (for CESM1 CAM4-chem grid) each month.

245 **2.4 DSMACC experiments**

Table 1 lists the experiments conducted with the DSMACC chemical box model. The reference
experiment (Ref_model in Table 1) is conducted by running the DSMACC model with the monthly mean
chemical species concentrations and meteorological conditions simulated by the 3D models (CESM1
CAM4-chem/ GEOSCCM) for each pixel in 2010 using the corresponding chemical mechanisms. During
250 the DSMACC simulation for each month, the meteorological conditions and chemical species with
lifetime from a few hours (e.g. NMVOCs) to several years (e.g. CH_4) are set to the monthly mean values
from 3D model outputs and unchanged during the simulation. We estimated the diurnal steady state

solution for the chemical species with short lifetime of a few seconds (e.g. OH and HO₂ radicals). Since most of the CCMi models provide the 3D distributions of the chemical species on monthly time resolution, the influence of sub-monthly variations such as the diurnal cycle for these chemical species and meteorological conditions on OH concentrations are not represented in the DSMACC simulations. In the All_obs simulation, the CO, NO₂, O₃, CH₄, and CH₂O, total column O₃, T_a, and H₂O_(g) are replaced with the available observation-based data for 2010, while other DSMACC inputs (pressure and other chemical species) are the same as in Ref_model simulation. For CO, CH₄, CH₂O, and meteorological conditions, the observation-based data are directly taken from the monthly mean of the assimilated/reanalysis data as described in section 2.2 (regrid to model horizontal and vertical grid). For tropospheric NO₂ and O₃, we use satellite data to generate the observation-based DSMACC input. The associated uncertainties of using the satellite observations of O₃ and NO₂ at overpass time are discussed in section 4.3. As the satellite observations provide the tropospheric VCDs, the observation-based concentrations are estimated by combining the satellite observed tropospheric columns and model simulated vertical distributions. We estimate the tropospheric column density simulated by atmospheric chemistry models (C_{trop_model}) using the tropopause pressure estimated based on the WMO tropopause definition (World Meteorological Organization, 1957). Then we estimate the scaling factor for each model horizontal grid cell as the ratio of satellite observations (C_{trop_obs}) to the modeled tropospheric column density (C_{trop_model}). The observation-based concentration (C_{grid_obs}) in each model pixel, which is used as the DSMACC input, is then estimated by multiplying the corresponding model simulated concentration (C_{grid_model}) by the scaling factor:

$$C_{grid_obs} = C_{grid_model} \times \frac{C_{trop_obs}}{C_{trop_model}} \quad (1)$$

For O₃, we estimate the C_{grid_obs} for each 3D model pixel in the whole troposphere using equation 1. For NO₂, we only estimate C_{grid_obs} in the boundary layer (the boundary layer height is from the MERRA-2 reanalysis data) since the NO₂ emitted from the surface mainly remains within the boundary layer.

The Ref_model experiments can well reproduce the spatial distribution of $[OH]_{\text{trop-M}}$ simulated by 3D models (Fig. S4), which indicate that the chemical box model DSMACC can generally capture the response of $[OH]$ to the changes in OH precursor concentrations and meteorological conditions. However, the Ref_model experiments overestimate the $[OH]_{\text{trop-M}}$ by 7% and 36% when compared with the global $[OH]_{\text{trop-M}}$ simulated by CESM1 CAM4-chem and GEOSCCM, respectively. Thus, the observation-based $[OH]$ ($[OH]_{\text{obs}}$) in each 3D model pixel for two different chemical mechanisms is estimated by correcting $[OH]$ as simulated by the corresponding 3D models ($[OH]_{\text{model}}$) by the ratio between $[OH]$ simulated by DSMACC experiments for the All_obs ($[OH]_{\text{DSMACC_all_obs}}$) and for the Ref_model ($[OH]_{\text{DSMACC_Ref_model}}$) case :

$$[OH]_{\text{obs}} = [OH]_{\text{model}} \times \frac{[OH]_{\text{DSMACC_all_obs}}}{[OH]_{\text{DSMACC_Ref_model}}} \quad (2)$$

Then, we also perform 8 sensitivity experiments (xk_obs in Table 1) that only adjust one individual chemical species or meteorological condition (here and after represented as x_k) to the observations (obs), keeping the other parameters equal to the simulated values from the chemistry-climate model. Because of high computing costs, we conduct the sensitivity experiments using only CESM1 CAM4-chem outputs. The OH biases due to each factor ($\delta[OH]_k$) are estimated by introducing the $[OH]$ simulated in the sensitivity experiment xk_obs ($[OH]_{\text{DSMACC_xk_obs}}$) as:

$$[OH]_{\text{xk_obs}} = [OH]_{\text{model}} \times \frac{[OH]_{\text{DSMACC_xk_obs}}}{[OH]_{\text{DSMACC_Ref_model}}} \quad (3)$$

$$\delta[OH]_{\text{xk}} = [OH]_{\text{model}} - [OH]_{\text{xk_obs}} \quad (4)$$

2.5 Chemical loss of CH₄

We estimate the yearly tropospheric chemical loss of CH₄ through reaction with OH (L_{CH_4+OH}) at global and regional scale from 2000 to 2009 by integrating the reaction of CH₄ with OH:

$$L_{CH_4+OH} = \sum_i \sum_t K(T_a) m(CH_4) [OH] \delta t \quad (4)$$

305 Where i is the index of the model pixel in the troposphere and δt is the integration time step (3 hours). The monthly 3D distributions of CH₄ mass ($m(CH_4)$) during 2000-2009 are from data assimilation of surface CH₄ observations from NOAA/ESRL (Dlugokencky et al., 1994) and the T_a distributions are from MERRA-2 reanalysis data (see Section 2.2). The reaction rate $K(T_a)$ is a function of T_a as given by Sander et al. (2011):

$$310 \quad K(T_a) = 2.45 \times 10^{-12} e^{-\frac{1775}{T_a}} \quad (5)$$

The contribution of each factor x_k to the bias in $\delta L_{CH_4+OH_{xk}}$ can be estimated as:

$$\delta L_{CH_4+OH_{xk}} = \sum_i \sum_t K(T) m(CH_4) \delta [OH]_{xk} \delta t \quad (6)$$

With L_{CH_4+OH} , we further estimate the CH₄ lifetime to reaction with tropospheric OH (τ_{CH_4+OH}) through the global CH₄ burden:

$$315 \quad \tau_{CH_4+OH} = \frac{\sum_j m(CH_4)}{L_{CH_4+OH}} \quad (7)$$

Where j is the index of the model pixel in the entire atmosphere.

3 Results

3.1 Observation-based tropospheric [OH]

3.1.1 Global tropospheric OH burden.

320 The global mean tropospheric column-averaged airmass-weighted [OH] ($[OH]_{\text{trop-M}}$) simulated by CESM1 CAM4-chem and GEOSCCM in 2010 are 11.9×10^5 molec cm⁻³ and 12.6×10^5 molec cm⁻³, respectively. By adjusting OH precursors and meteorological conditions (total column O₃, tropospheric O₃, CO, CH₄, CH₂O, boundary layer NO₂, H₂O_(g), and T_a) to the observations using the DSMACC model, we estimated the observation-based $[OH]_{\text{trop-M}}$ to be 9.9×10^5 molec cm⁻³ and 10.4×10^5 molec cm⁻³ with

325 CESM1 CAM4-chem and GEOSCCM chemical mechanisms, respectively (Fig.1 and Table 2). Compared
with the original OH fields simulated by CESM1 CAM4-chem and GEOSCCM, the observation-based
OH fields reduce the model-simulated global $[\text{OH}]_{\text{trop-M}}$ by $\sim 2 \times 10^5 \text{ molec cm}^{-3}$. The global $[\text{OH}]_{\text{trop-M}}$
estimated by the observation-based OH fields in this study is lower than the value estimated by
330 Spivakovsky et al. (2000) ($11.6 \times 10^5 \text{ molec cm}^{-3}$), which is used in the chemistry-transport model (CTM)
intercomparison experiment (TransCom-CH4) after scaled by a factor of 0.92 (Patra et al., 2011), but
consistent with those estimated by MCF-based inversions ($\sim 10 \times 10^5 \text{ molec cm}^{-3}$; Bousquet et al., 2005;
Krol and Lelieveld, 2003). The consistency with the MCF-based estimates indicates that our approach
(correcting model bias through available observations) is capable of capturing the global OH burden.

335 **3.1.2 The OH spatial distribution.**

Fig. 1 and Fig. 2 show the spatial distribution and zonal average of the $[\text{OH}]_{\text{trop-M}}$, respectively, estimated
from the observation-based and original model simulated OH fields. The observation-based OH fields
show similar spatial distributions as their respective original model simulations, with high $[\text{OH}]_{\text{trop-M}}$ (10 -
 $15 \times 10^5 \text{ molec cm}^{-3}$) over East Asia, South Asia, and Northern Africa, corresponding to the regions with
340 high tropospheric O_3 , NO_2 , and $\text{H}_2\text{O}_{(\text{g})}$ (Fig. S1 and Fig. S3). The lowest $[\text{OH}]_{\text{trop-M}}$ is found over the high
latitudes ($< 4 \times 10^5 \text{ molec cm}^{-3}$) due to less ultraviolet radiation and over the Amazon forest (4 - $8 \times 10^5 \text{ molec}$
 cm^{-3}) due to high biogenic non-methane volatile organic compounds (NMVOC) emissions. The
observation-based $[\text{OH}]_{\text{trop-M}}$ averaged over the northern tropics (0 - 30°N) and northern mid-to-high
latitudes (30 - 90°N) are $> 14 \times 10^5 \text{ molec cm}^{-3}$ and $> 7 \times 10^5 \text{ molec cm}^{-3}$, respectively, for both chemical
345 mechanisms, which are higher than those over the southern tropics (12.2 - $13.6 \times 10^5 \text{ molec cm}^{-3}$) and
southern mid-to-high-latitudes (5.3 - $5.6 \times 10^5 \text{ molec cm}^{-3}$, Table 3 and Fig. 2). The two observation-based

OH fields show similar mean $[\text{OH}]_{\text{trop-M}}$ over most of the latitudinal bands except for the southern tropics (0-30°S), where the mean $[\text{OH}]_{\text{trop-M}}$ estimated by the GEOSCCM chemical mechanism is $1.4 \times 10^5 \text{ molec cm}^{-3}$ higher than the one from CESM1 CAM4-chem (Table 3 and Fig. 2).

350

Compared to the original $[\text{OH}]_{\text{trop-M}}$ simulated by CESM1 CAM4-chem and GEOSCCM, adjusting to observations reduces the $[\text{OH}]_{\text{trop-M}}$ by $2-8 \times 10^5 \text{ molec cm}^{-3}$ over most regions except the tropical forests. The reduction of mean $[\text{OH}]_{\text{trop-M}}$ over the northern tropics (0°-30°N) and mid-to-high latitudes (30°-90°N) are $>3 \times 10^5 \text{ molec cm}^{-3}$ and $>2 \times 10^5 \text{ molec cm}^{-3}$, respectively, which is larger than that over the southern tropics (0°-30°S, by $\sim 2 \times 10^5 \text{ molec cm}^{-3}$) and mid-to-high latitudes (30°-90°S, by $0.6 \times 10^5 \text{ molec cm}^{-3}$). The Northern Hemisphere to Southern Hemisphere (N/S) ratios of the simulated OH fields are reduced from 1.35 to 1.24 for CESM1 CAM4-chem, and 1.26 to 1.15 for GEOSCCM. Although the N/S ratios of the observation-based OH fields are still higher than the 1, which is obtained from MCF-based inversions (Bousquet et al., 2005; Patra et al., 2014), incorporating available observations has significantly reduced the model simulated N/S ratio.

360

The spatial distribution of the observation-based $[\text{OH}]$ of this study is different from the OH field estimated by Spivakovsky et al. (2000). The OH field estimated by Spivakovsky et al. (2000) OH field shows a high $[\text{OH}]_{\text{trop-M}}$ over the regions with biomass burning emissions (Fig. S5). Instead of considering the detailed spatial distributions of nitrogen oxides, Spivakovsky et al. (2000) use a series of NO_y profiles for land and ocean over large regions (Fig. S6). As shown in Fig. S5 and Fig. S6, the highest $[\text{OH}]_{\text{trop-M}}$ over South America and Africa estimated by Spivakovsky et al. (2000) correspond to high NO_y mixing ratios over these two regions. The $[\text{OH}]$ shows high positive sensitivity to NO_y in the free troposphere, due to low VOCs and NO_t mixing ratios (Fig. S7). Using satellite observations, Choi et al. (2014) showed that the high NO_2 mixing ratios in the free troposphere are mainly located near polluted urban regions

370

(e.g., North America, Europe, and Asia), which is more similar to the NO_2 distribution simulated by 3D atmospheric models (Fig. S1). Thus, although the OH field estimated by Spivakovsky et al. (2000) gives an N/S ratio of 1, its spatial distribution may have biases due to the simplification in the NO_t distributions.

375 **3.2 Contribution from individual factors to model biases in $[\text{OH}]_{\text{trop-M}}$**

By conducting the sensitivity simulations listed in Table 1, we estimate the contribution of individual factors to model biases based on Equation 3-4. The sensitivity of OH to model biases in tropospheric O_3 , stratospheric O_3 , $\text{H}_2\text{O}_{(\text{g})}$, and NO_x emissions have been tested in Strode et al. (2015) using GEOSCCM. In this Section, we extend the procedure of Strode et al. (2015) by including more factors: T_a , CO, CH_2O ,
380 CH_4 , and NO_2 in the boundary layer.

Table 4 summarizes the contribution of each chemical precursor and meteorological condition to the difference between CESM1 CAM4-chem simulated and observation-based global $[\text{OH}]_{\text{trop-M}}$. On the global scale, the total contribution of the 8 individual factors to the difference in $[\text{OH}]_{\text{trop-M}}$ estimated
385 from the simulation `xk_obs` is $2.0 \times 10^5 \text{ molec cm}^{-3}$ (Table 4), consistent with that estimated from the simulation `All_obs` (Table 2). On the regional scale, they show small differences (usually $<10\%$ of the signal, Fig. S8), which can be attributed to the nonlinear chemistry. Indeed, although the atmospheric OH is produced and removed through complex nonlinear chemical reactions, one can infer the large-scale $[\text{OH}]_{\text{trop-M}}$ changes by roughly summing the influence from individual factors.

390

3.2.1 Contribution from CO

CO is the largest OH sink in the troposphere (Lelieveld et al., 2016; Zhao et al., 2020b). The sensitivity simulation `CO_obs` shows that a 1 ppbv increase in CO can result in a decrease in $[\text{OH}]$ by up to more than $3 \times 10^4 \text{ molec cm}^{-3}$ (Fig. S7). Compared with the CO distributions from inversions that assimilated

395 MOPITT observations, the CESM1 CAM4-chem underestimates the global tropospheric mean CO
mixing ratio by 24 ppbv (Fig. S1). Based on the DSMACC simulations CO_obs and Ref_CESM (Table
1), we find that the negative bias in CO contributes most to the difference in the modeled versus
observation-based $[\text{OH}]_{\text{trop-M}}$ ($1.3 \times 10^5 \text{ molec cm}^{-3}$; Table 4 and Fig. 3). The underestimation of CO is
common in atmospheric models and was treated either as a cause or an effect of the overestimated $[\text{OH}]$
400 in previous studies (Naik et al., 2013; Monks et al. 2015; Stode et al., 2015). For example, based on the
ACCMIP simulations, Naik et al. (2013) found that the positive bias in $[\text{OH}]$ was most likely due to the
underestimation of CO when compared with both satellite and surface observations. In contrast, Stode
et al. (2015) did sensitivity simulations using the GEOSCCM model and showed that reducing OH bias
could improve the accuracy of modeled CO. In this study, we do not intend to solve the cause/effect issue
405 between CO and OH, since the discrepancy in $[\text{OH}]_{\text{trop-M}}$ of $1.3 \times 10^5 \text{ molec cm}^{-3}$ could also be understood
as the global tropospheric $[\text{OH}]$ changes that would be needed to simulate the observed CO.

The underestimation of the CO mixing ratio is larger over the Northern Hemisphere (30 ppbv) than over
the Southern Hemisphere (18 ppbv) (Fig. S1). The largest bias in $[\text{OH}]_{\text{trop-M}}$ induced by CO is found over
410 the northern tropics ($1.9 \times 10^5 \text{ molec cm}^{-3}$) followed by those over the northern mid-to-high latitude regions
and the southern tropics ($1.2 \times 10^5 \text{ molec cm}^{-3}$; Table 4 and Fig. 2). Naik et al. (2013) demonstrated that
the model bias in CO contributes to the overestimation of the modeled N/S ratio in $[\text{OH}]_{\text{trop-M}}$. In this
study, although the underestimation of CO leads to a larger positive bias of $[\text{OH}]_{\text{trop-M}}$ over the Northern
Hemisphere than the Southern Hemisphere, the observation-based adjustment only reduces the positive
415 bias of the N/S ratio by 0.02. This means that the N/S difference of the CO bias is not sufficient to explain
the inconsistency between the CESM1 CAM4-chem simulated and MCF-based N/S ratio in $[\text{OH}]_{\text{trop-M}}$.

3.2.2 Contribution from tropospheric O₃

Tropospheric O₃ can contribute to both primary and secondary OH production. Compared to satellite
420 observations from OMI, CESM1 CAM4-chem simulations show a large overestimation of tropospheric
O₃ over the 15-60°N region (up to 14 DU, 40%) and an underestimation (14 DU, 40%) over the tropics
and Southern Hemisphere (Fig. S1).

At the global scale, the model bias in O₃ leads to a negative bias on [OH]_{trop-M} by 0.3×10^5 molec cm⁻³,
425 much smaller than that caused by CO (Table 4). However, at the regional scale, The CESM1 CAM4-chem
simulated [OH]_{trop-M} is enhanced by $\sim 1 \times 10^5$ molec cm⁻³ over the tropics (15°S-15°N) and $\sim 0.5 \times 10^5$ molec
cm⁻³ over the mid-southern hemisphere (15°-60°S), while it is reduced by $0.1-0.3 \times 10^5$ molec cm⁻³ over
the mid-northern hemisphere (15°-60°N) when adjusted to OMI/MLS tropospheric column O₃ (Fig. 2).
The adjustment reduces the N/S ratio of [OH]_{trop-M} by 0.07, but still cannot explain the overestimation of
430 the N/S ratio but leads to a larger correction than the one with CO alone.

3.2.3 Contribution from boundary layer NO₂.

The sensitivity of OH to NO₂ is highly variable. We estimate that a 1 ppbv increase in NO₂ can lead to a
change of [OH] ranging from -3×10^6 molec cm⁻³ to more than $+10 \times 10^6$ molec cm⁻³, depending on the
435 mixing ratio of NMVOCs (represented as HCHO+isoprene) and NO₂ (Fig. S7). Compared to the
QA4ECV NO₂ retrieval product, CESM CAM-Chem overestimates tropospheric NO₂ over most regions
except North China and tropical forests (Fig. S1).

At the global scale, the overestimation of NO₂ leads to a positive bias in [OH]_{trop-M} by 0.3×10^5 molec cm⁻³
440 (Table 4). At the regional scale, correcting for the PBL NO₂ does not influence the N/S ratio of OH. As

shown in Fig. 3, the overestimation of PBL NO₂ results in a positive bias in [OH]_{trop-M} over most of the continental regions. Over tropical and temperate oceans, one can also see that the slight overestimation in NO₂ leads to a significant positive bias in OH by $0.5-1 \times 10^5$ molec cm⁻³ since the sensitivity of [OH]_{trop-M} to NO₂ can be very high (10^7 molec cm⁻³/ ppbv NO₂) over the regions with low NO_x and NMVOC mixing ratios. Over northern China, although the model shows a large underestimation in NO₂ (Fig. S1), the [OH]_{trop-M} is slightly smaller after adjustment. This is because over high NO₂ regions, the [OH] is not sensitive to an increase in NO₂ or even shows a negative response (Fig. S7).

3.2.4 Contribution from total column O₃

Total column O₃ mainly influences O¹(D) photolysis through absorbing UV radiation. The CESM1 CAM4-chem simulation mainly underestimates the total O₃ columns by up to ~10 DU over tropical regions compared with the SBUV/MOD observations (Fig. S2). On a global scale, the underestimation of the O₃ total column can lead to an overestimation of the [OH]_{trop-M} by $\sim 0.6 \times 10^5$ molec cm⁻³ (Fig. 2 and Fig. 3), comparable with that due to tropospheric O₃.

3.2.5 Contribution from CH₄ and CH₂O

In CCMI-1 simulations, atmospheric chemistry models prescribe the lower boundary conditions for CH₄ following the Representative Concentration Pathway (RCP6.0). Compared to the posterior CH₄ fields from inversions by assimilating the surface CH₄ observations, the tropospheric mean CH₄ mixing ratios used in the CESM CAM4-chem are ~80 ppbv lower over the tropical and extratropical regions with high biomass burning and anthropogenic emissions, and ~40 ppbv lower over other regions. But due to the low sensitivity of [OH] to CH₄ changes (Fig. S1), the underestimation in CH₄ only leads to a small positive bias in the global tropospheric mean [OH] by 0.1×10^5 molec cm⁻³.

465 CESM CAM4-chem overestimates CH₂O by more than 50% over land but slightly underestimates CH₂O over tropical oceans (Fig. S1). Since the CH₂O contributes to only a small part (6%) of the total [OH] loss (Zhao et al., 2020b), the large bias in the CESM CAM4-Chem simulated CH₂O only leads to a small positive bias global mean [OH]_{trop-M} by 0.1×10^5 molec cm⁻³ (Fig.3).

470 **3.2.6 Contribution from meteorological conditions**

H₂O_(g) is a major OH precursor that contributes to the primary production of OH and T_a can influence OH production and loss rates. Compared to MERRA2 reanalysis data, CESM CAM4-chem overestimates zonally averaged H₂O_(g) mixing ratios near the surface and around 800 hPa by ~1.5g/kg (Fig. S3). The sensitivity experiments show that a change in specific humidity by 1g/kg can lead to a change in [OH] 475 by $>3 \times 10^5$ molec cm⁻³ over the regions with high O(¹D) photolysis and low NMVOC mixing ratios (Fig. S6). As shown in Table 4 and Fig.3, globally, the model bias in H₂O_(g) only leads to a small bias (0.1×10^5 molec cm⁻³) in [OH]_{trop-M}, but regionally, the model bias in H₂O_(g) can lead to a bias in [OH]_{trop-M} by the magnitude of 5.0×10^5 molec cm⁻³, even larger than that induced by the bias in CO. For T_a, the model only shows a small bias (<1°C) compared with MERRA2 reanalysis data (Fig. S3). Thus, model bias in 480 [OH]_{trop-M} induced by T_a is negligible (Fig. 3).

3.3 Chemical sinks of CH₄ as estimated by observation-based OH fields

3.3.1 Global and regional OH chemical sink of CH₄

Using the observation-based OH field, we estimate that the global tropospheric CH₄ loss by reaction with 485 tropospheric OH (L_{CH₄+OH}) averaged during the period 2000 through 2009 is 434 Tg yr⁻¹ and 461 Tg yr⁻¹ for CESM1 CAM4-chem and GEOSCCM, respectively. These estimates are about 105 Tg yr⁻¹ lower than

estimated by the original model simulated OH fields (540 Tg yr⁻¹ and 565 Tg yr⁻¹, respectively; Table 2). The corresponding CH₄ lifetimes against tropospheric OH loss estimated by the two observation-based OH fields are 11.4 yr and 10.7 yr for CESM1 CAM4-chem and GEOSCCM, respectively, well within the
490 range estimated by Prather et al. (2012) based on the MCF-inversions (11.2±1.3yr) and much longer than estimated by the original model simulated OH fields (9.1 yr for CESM1 CAM4-chem and 8.7 yr for GEOSCCM).

As shown in Table 3, more than 70% of the tropospheric L_{CH₄+OH} occurs over tropical regions mainly due
495 to both high [OH] and T_a. Constraining the tropospheric [OH] by precursor concentrations reduces the tropospheric L_{CH₄+OH} by ~30 Tg yr⁻¹ (16%) over the southern tropics, ~50 Tg yr⁻¹(21%) over the northern tropics, and ~25 Tg yr⁻¹(25%) over the northern mid-to-high latitude as estimated by both CESM1 CAM4-chem and GEOSCCM OH fields. Over the southern mid-to-high latitude regions, there are only limited changes (6 Tg yr⁻¹) in tropospheric L_{CH₄+OH}. Thus, constraining tropospheric [OH] by precursor
500 concentrations changes the inter-hemispheric distribution of L_{CH₄+OH}. The values of L_{CH₄+OH} estimated by the observation-based OH fields are ~35 Tg yr⁻¹ and ~75 Tg yr⁻¹ lower than that estimated by the corresponding original model simulated OH fields over the Southern and Northern Hemispheres, respectively (Table 3). Thus, the inter-hemispheric difference of L_{CH₄+OH} (north – south) estimated by
505 observation-based OH fields (60 Tg yr⁻¹ by CESM1 CAM4-chem and 48 Tg yr⁻¹ by GEOSCCM) is ~40% lower than estimated by the original model simulated OH fields (98 Tg yr⁻¹ by CESM1 CAM4-chem and 81 Tg yr⁻¹ by GEOSCCM).

3.3.2 Global total chemical sink of CH₄

We estimate the global total CH₄ chemical sink for 2000-2009 by gathering: (1) the tropospheric L_{CH₄+OH}
510 estimated using the original model-simulated and observation-based OH fields, (2) the CH₄ loss in the

stratosphere (26 Tg yr⁻¹ estimated by CESM1 CAM4-chem and 36 Tg yr⁻¹ estimated by GEOSCCM simulations) and CH₄ oxidated by chlorine (11 Tg yr⁻¹) given by Saunois et al. (2020). We then compare the chemical sink estimated in this study with that estimated by the bottom-up and top-down methods given by previous GCP global CH₄ budget (Saunois et al., 2016; 2020).

515

As shown in Fig. 4, the bottom-up estimates in the GCP global CH₄ budget (blue bars) have a large range (483-738 Tg yr⁻¹ in Saunois et al. (2016) and 489-779 Tg yr⁻¹ in Saunois et al. (2020)), much higher than those from the top-down method (514 Tg yr⁻¹ in Saunois et al. (2016) and 459-516 Tg yr⁻¹ in Saunois et al. (2020)). The CH₄ sinks simulated by CESM1 CAM4-chem (549 Tg yr⁻¹) and GEOSCCM (585 Tg yr⁻¹) were included in the bottom-up estimates in Saunois et al. (2020) (green bar) and is slightly lower than the average value estimated using different OH fields (595 Tg yr⁻¹).

520

In this study, the global total CH₄ chemical sinks estimated using the originally simulated tropospheric OH and constrained CH₄ mixing ratios are 577 Tg yr⁻¹ and 612 Tg yr⁻¹ for CESM1 CAM4-chem and GEOSCCM for 2000-2009, respectively, close to the mean values estimated by the bottom-up method (around 600 Tg yr⁻¹) using different OH fields but much higher than the top-down estimates (around 500 Tg yr⁻¹). It should be noted that the bottom-up estimates of the chemical loss of CH₄ in the previous GCP, global CH₄ sinks were calculated using model-simulated CH₄ mixing ratios (Fig.4; Saunois et al. 2020). The CH₄ mixing ratios simulated by CESM1 CAM4-chem and GEOSCCM are lower than that used in this study (Fig. S1). Thus, the chemical sink of CH₄ estimated in this study is higher than that estimated in Saunois et al. (2020) by ~30 Tg yr⁻¹. After adjusting the main OH precursors to observations, the global chemical sink of CH₄ for 2000-2009 is 471-508 Tg yr⁻¹, as estimated using the two observation-based OH fields, more consistent with top-down method estimates (~500Tg yr⁻¹).

530

535 The above analyses show that the large uncertainties in the bottom-up estimates of the CH₄ chemical sink are attributable to the use of the model-simulated OH fields with known biases. Constraining the OH field with available precursor observations to correct the global [OH], the magnitude of the methane loss is more in line with top-down methane inversions. Therefore, we partly reconcile the bottom-up and top-down estimates of the CH₄ sink. Although only two of seven bottom-up models synthesized in Saunio et al. (2020) are considered in this study, our approach can be generalized to other chemistry-climate models. 540 Instead of directly using the OH fields simulated from an atmospheric chemistry model, the bottom-up estimates can use the precursor observations and box-model based approach proposed here to reduce model biases of OH fields.

545 **3.3.3 Contribution from the model biases of individual OH precursors to chemical sink of CH₄**

We further quantify the influence of model biases in individual OH precursors on the bottom-up estimates of CH₄ chemical sink ($\delta L_{\text{CH}_4+\text{OH}_{\text{sk}}}$). At the global scale, the underestimation of CO and total column O₃ and the overestimation of NO₂ by the CESM1 CAM4-chem lead to a positive bias of 60 Tg yr⁻¹(11%), 22 Tg yr⁻¹(4%), and 22 Tg yr⁻¹ (4%) in tropospheric L_{CH₄+OH} (Fig.4 and Table 4), respectively, while an 550 underestimation of tropospheric O₃ leads to a negative bias of 17 Tg yr⁻¹ (3%) in tropospheric L_{CH₄+OH}. Although the model bias of [OH]_{trop-M} induced by H₂O_(g) is negligible on the global scale, the observation-based adjustment of H₂O_(g) leads to a reduction in tropospheric L_{CH₄+OH} by 10 Tg (2%), since the model overestimation of H₂O_(g) is concentrated over the mid-to-low latitude regions where tropospheric CH₄ oxidation mainly occurs (Fig. S3). The model bias in CH₂O and CH₄ itself leads to a small positive bias 555 of ~1% respectively on L_{CH₄+OH}.

As the tropospheric L_{CH₄+OH} mainly occurs over the mid-to-low latitude regions, the biases in [OH]_{trop-M} over the high latitudes (north of 60°N or south of 60°S) due to an overestimation of CO and

underestimation of $\text{H}_2\text{O}_{(\text{g})}$, do not substantively contribute to the bias in $L_{\text{CH}_4+\text{OH}}$ (Fig. 2). Over the regions
560 north of 15°N , nearly all the precursors considered in this study contribute to the overestimation of
 $L_{\text{CH}_4+\text{OH}}$ (55 Tg yr^{-1} in total), of which 47% (26 Tg yr^{-1}) is contributed by model underestimation of CO.
South of 15°N , the underestimation of tropospheric O_3 results in an underestimation of $L_{\text{CH}_4+\text{OH}}$ by 22 Tg
 yr^{-1} , partly offsetting the overestimation of $L_{\text{CH}_4+\text{OH}}$ induced by CO (34 Tg yr^{-1}) and other precursors (40
 Tg yr^{-1} in total) (Fig. 2). As aforementioned, the inter-hemispheric difference of $L_{\text{CH}_4+\text{OH}}$ derived from the
565 observation-based OH fields is 48 Tg yr^{-1} smaller than estimated using the OH field originally simulated
by CESM1 CAM4-chem. The biases in CO, tropospheric O_3 , and boundary layer NO_2 , lead to an
overestimation of the inter-hemispheric difference of tropospheric $L_{\text{CH}_4+\text{OH}}$ by 15 Tg yr^{-1} , 15 Tg yr^{-1} , and
 9 Tg yr^{-1} , respectively, dominating the bias in the inter-hemispheric difference in tropospheric $L_{\text{CH}_4+\text{OH}}$.

570 **4 Conclusions and discussion**

In this study, we aim to reconcile the top-down and bottom-up estimates of the major global CH_4 sink and
to quantify the contribution of each factor to the overestimation of tropospheric $[\text{OH}]$ that is generally
found in atmospheric chemistry models and to the consequent overestimation of CH_4 chemical loss in the
575 bottom-up studies. To do so, we propose a new approach based on precursor observations and a chemical
box model, to improve the 3D distributions of tropospheric OH radicals issued from atmospheric
chemistry models.

4.1 Conclusions for $[\text{OH}]$.

580 We estimate two 3D observation-based OH fields based on three components: (i) simulated tropospheric
 $[\text{OH}]$ and related chemical species from global 3D atmospheric chemistry models (here CESM1-
CAM4chem and GEOSCCM), (ii) sensitivities of tropospheric $[\text{OH}]$ to its precursors in each model grid

cell estimated by the chemical box model DSMACC using a chemical mechanism similar to the 3D model, and (iii) observations of chemical species related to OH production and loss (CO, O₃, boundary layer NO₂, CH₄, CH₂O, and total column O₃) and meteorological conditions (H₂O_(g) and T_a). The chemical box model DSMACC can be compiled using different chemical mechanisms, making it possible to apply this approach to other atmospheric chemistry models and improve their representation of [OH].

The global [OH]_{trop-M} estimated from observation-based OH fields is $\sim 10 \times 10^5$ molec cm⁻³ in 2010 based on two different chemical mechanisms, which is 2×10^5 molec cm⁻³ lower than the original model-simulated global [OH]_{trop-M}, consequently reaching consistency with the value derived by MCF-based inversions (around 10×10^5 molec cm⁻³; Bousquet et al., 2005; Krol and Lelieveld, 2003). The observation-based adjustments also change the latitudinal distribution of [OH], reducing the its north to south ratios from 1.35 and 1.26 to 1.24 and 1.15 for CESM1 CAM4-chem and GEOSCCM, respectively, closer to, albeit not as low as the one obtained from MCF-based inversions (slightly smaller than 1).

Based on the simulations from CESM1 CAM4-chem, globally, the overestimation of [OH]_{trop-M} arises mainly from the underestimation of CO and total column O₃, and the overestimation of boundary layer NO₂, which contribute 1.3×10^5 molec cm⁻³, 0.4×10^5 molec cm⁻³, and 0.3×10^5 molec cm⁻³, respectively, to the bias in [OH]_{trop-M}. For the N/S ratio of [OH]_{trop-M}, the positive bias in [OH]_{trop-M} over the Northern Hemisphere ($0.1-0.3 \times 10^5$ molec cm⁻³) and the negative bias over the tropics and Southern Hemisphere ($0.5-1.0 \times 10^5$ molec cm⁻³) due to tropospheric O₃ dominate the higher N/S ratio of [OH]_{trop-M} estimated by the CESM1 CAM4-chem than the observation-based OH field. At the regional scale, the model bias in H₂O_(g) can lead to bias in [OH]_{trop-M} even larger than that induced by CO.

605

4.2 Conclusions for the CH₄ sink

The global CH₄ loss by reaction with tropospheric OH ($L_{\text{CH}_4+\text{OH}}$) estimated from the observation-based OH fields is 434 Tg yr⁻¹ and 461 Tg yr⁻¹ for CESM1 CAM4-chem GEOSCCM, respectively, averaged over 2000 to 2009, which is lower than that estimated from the original model simulated OH fields by around 105 Tg yr⁻¹. Based on the results from CESM1 CAM4-chem, at the global scale, the underestimation of CO and total column O₃, and overestimation of NO₂ lead to positive biases in tropospheric $L_{\text{CH}_4+\text{OH}}$ by 60 Tg yr⁻¹(11%), 22 Tg yr⁻¹(4%), and 22 Tg yr⁻¹(4%), respectively, while an underestimation of tropospheric O₃ leads to a negative bias in tropospheric $L_{\text{CH}_4+\text{OH}}$ by 17 Tg yr⁻¹(3%). The inter-hemispheric difference in the tropospheric $L_{\text{CH}_4+\text{OH}}$ is therefore reduced by 40% (around 35 Tg yr⁻¹) when estimated using the observation-based OH field. Although the bias in the N/S ratio of $[\text{OH}]_{\text{trop-M}}$ is dominated by the tropospheric O₃ concentration, the positive bias in the inter-hemispheric difference of $L_{\text{CH}_4+\text{OH}}$ is determined together by the biases in CO (15 Tg yr⁻¹), tropospheric O₃ (15 Tg yr⁻¹), and boundary layer NO₂ (9 Tg yr⁻¹).

Using the tropospheric $L_{\text{CH}_4+\text{OH}}$ estimated with our observation-based OH fields, the global total CH₄ chemical sink is 471-508 Tg yr⁻¹. This quantification is more consistent with top-down estimates in the previous GCP global CH₄ budget (459-516 Tg yr⁻¹, Saunois et al., 2016; 2020) than it was before the adjustment (577-612 Tg yr⁻¹). The bottom-up method in the previous GCP global CH₄ budget estimated the CH₄ chemical sink directly using the OH fields simulated by atmospheric chemistry models. However, the uncertainties in the model simulated OH lead to an unreliable range in the bottom-up estimated CH₄ chemical sink, much higher than that estimated by the top-down method. Our results highlight that constraining the OH fields using available precursor observations can improve the bottom-up estimates of the CH₄ sink and help reconcile the difference between the top-down and bottom-up estimates of the CH₄ sink.

4.3 Discussion

Although the observation-based 3D OH fields presented in this study can capture the global tropospheric OH burden and chemical loss of CH₄, unresolved uncertainties and limitations remain:

635 (1) The method presented in this study cannot improve the chemical mechanisms in the models and does not fully explain the overestimation of the N/S ratios of [OH].

The differences in global [OH]_{trop-M} between the two observation-based OH fields estimated from CESM1 CAM4-chem and GEOSCCM simulations is 0.6×10^5 molec cm⁻³. Besides precursor concentrations, the inter-model difference in tropospheric [OH] is partly attributable to their differences
640 in chemical mechanisms (Nicely et al., 2018; 2020). As discussed by Murray et al. (2021), the oxidative efficiency of NMVOCs and lifetime of NO_x simulated by different models can largely determine inter-model differences in tropospheric [OH] and their responses to changes in precursors. Reducing the uncertainties due to the modeled chemical mechanisms relies on additional observations to improve the simulation of NMVOCs oxidative efficiency and NO_x lifetime, which is beyond the scope of our study.

645 The N/S ratio of [OH]_{trop-M} after observation-based adjustment is still higher than the one obtained from MCF-inversions (less than 1.0). This difference indicates that the overestimation of the N/S ratio by atmospheric models cannot be fully explained by the underestimation of CO and overestimation of O₃ over the Northern Hemisphere as mentioned in previous studies (Naik et al. 2013). The overestimation of
650 the N/S ratio may also be attributable to chemical mechanisms included in the atmospheric chemistry models. Both CESM1-CAM4chem and GEOSCCM do not include the OH recycling by isoprene and simulate low OH values in regions with high NMVOC emissions, such as rain forests in the Southern Hemisphere (Zhao et al., 2019). Including the chemical mechanism such as OH recycling by isoprene (Lelieveld et al. 2008) would help further reduce the N/S ratio for model-simulated OH fields.

(2) The constraints brought on tropospheric [OH] are limited by observations quality and time resolution of available model outputs.

Data constraining the OH precursors come mainly from satellite observations and reanalysis data, of which the uncertainties are not considered in this study. For example, the MERRA-2 reanalysis data significantly overestimate $\text{H}_2\text{O}_{(\text{g})}$ in the upper troposphere (Jiang et al., 2015); The QA4ECV tropospheric NO_2 vertical column density is lower compared with surface observations under the extremely high-pollution case compared with surface observations (Compernelle et al., 2020). The performance of this method depends on the accuracy of observations used to constrain individual factors. Data products regularly improve and, since the sensitivity of [OH] to each precursor is estimated by the chemical box model, we can easily improve the [OH] using the updated observational datasets.

OMI measures concentrations of chemical species around local time 13:30, but most of the CCMI models only provide monthly means for 3D distribution of chemical concentrations. The monthly mean NO_2 and O_3 concentrations simulated by 3D models are therefore constrained only by such afternoon observations. For O_3 , of which the tropospheric mean lifetime is 23.4 ± 2.2 days (Young et al., 2013), we assume that not considering diurnal variations has only a small influence. This is not the case for NO_2 with a much shorter lifetime (~ 1 day, Jaffe et al., 2003). By comparing the tropospheric NO_2 VCDs observed by SCIAMACHY (SCanning Imaging Absorption SpectroMeter for Atmospheric Chartography; overpass time around local time 10:00) with OMI, previous studies show that the tropospheric NO_2 VCDs have significant diurnal variations (Boersma et al., 2008; 2009). Diurnal variations of NO_2 VCDs are controlled by complex factors including local emissions, photochemistry, deposition, advection, etc., and vary among different seasons over different regions (Boersma et al., 2008; 2009). Considering the diurnal cycle

of NO₂ photolysis, tropospheric NO₂ VCDs over remote regions should be lower during daytime than
680 nighttime (Cheng et al., 2019). Constraining the model simulated monthly mean NO₂ VCDs with satellite
data at the overpass time leads to an overestimation of the high bias of modeled tropospheric NO₂ VCDs.
Thus, the 0.3×10^5 molec cm⁻³ estimated in this study gives an upper limit of the high bias in global
[OH]_{trop-M} due to boundary layer NO₂.

685 Since we only have the tropospheric NO₂ VCDs, another key factor that could influence the tropospheric
OH burden but is unconstrained in this study is NO₂ in the free troposphere. Although the NO₂ mixing
ratio is usually less than 1 ppbv in the free troposphere, the sensitivity of [OH] to NO₂ can be very high
in low NO₂ regions. However, a potential model bias due to lightning NO_x emissions, which had proven
to contribute significantly to the upper-tropospheric [OH] burden (Murray et al., 2013; Turner et al., 2018),
690 is not adjusted in our study. Satellite retrievals for upper tropospheric NO₂ (e.g. Belmonte Rivas et al.,
2015; Marais et al., 2021) could help quantify [OH] biases due to free tropospheric NO₂ and the
contribution of lightning NO_x emissions.

4.4 Future developments

695 The new approach proposed here to improve the 3D OH fields and chemical loss of CH₄ can be applied
broadly. It relies on observations of OH precursor concentrations that can be applied efficiently to any
atmospheric chemistry model with a box-model (0D) available. Here we only apply this method to two
models for one year (2010) and both of them agree with MCF-based inversions in terms of the global OH
burden. One future research development is to generate observation-based OH fields for all the
700 atmospheric chemistry models included in the GCP global CH₄ budget and over a longer time period,
especially for the models that simulate extremely high or low [OH]. This will allow us to see if our results
can be generalized with a larger range of [OH] and CH₄ losses and to see if a higher consistency can also

be achieved on longer timescales. It will also be important to assess how much uncertainty in [OH] means and trends can be further reduced and achieved in detail.

705

The CH₄ emissions from top-down approaches used mostly a single OH field from Spivakosky (2000), which relies on climatological data without any interannual variations. Some CH₄-inversions used the OH fields from chemistry-climate or chemistry-transport models with the known aforementioned biases that may lead to bias in the inverted surface CH₄ fluxes. Our OH product could be used instead in CH₄ inversions to better infer CH₄ emissions and reduce the uncertainties in the global methane budget. Each modeling group could also generate their own corrected OH for the purpose of methane atmospheric inversions. Further work is necessary to consider the interannual changes in our observation-based estimates.

710

715 **Data availability**

The GEOSCCM OH fields are available at the Centre for Environmental Data Analysis (CEDA; <http://data.ceda.ac.uk/badc/wcrp-ccmi/data/CCMI-1/output>; last access: December 2019, Hegglin and Lamarque, 2015), the Natural Environment Research Council's Data Repository for Atmospheric Science and Earth Observation. The CESM1 CAM4-chem outputs for CCMI are available at <http://www.earthsystemgrid.org> (Climate Data Gateway at NCAR, last access: December 2019).

720

Code availability

The DSMACC model code and descriptions are available at http://wiki.seas.harvard.edu/geos-chem/index.php/Main_Page.

725

Author contributions

YZ, MS, and PB designed the study, analyzed data, and wrote the manuscript. XL helped with data preparation. JGC and RBJ provided input into the study design and discussed the results. MIH provided CCMI model outputs. BZ provided the assimilated CO and CH₂O distributions. All co-authors commented on the manuscript.

Acknowledgements

This work benefited from and is a contribution to the Global Methane Budget activity of the Global Carbon Project.

We acknowledge the modeling groups for making their simulations available for this analysis, the joint WCRP SPARC/IGAC Chemistry–Climate Model Initiative (CCMI) for organizing and coordinating the model simulations and data analysis activity, and the British Atmospheric Data Centre (BADC) for collecting and archiving the CCMI model output. JGC acknowledges support from the National Environmental Science Program – Climate Systems Hub. RBJ acknowledges the U.N. Environment Programme for support of the Global Methane Budget.

Competing interests

The authors declare that they have no conflicts of interest.

Financial support

This research has been supported by Shandong Provincial Natural Science Foundation (grant no. 2022HWYQ-066) and the Gordon and Betty Moore Foundation (grant no. GBMF5439), “Advancing Understanding of the Global Methane Cycle”, and the U.N. Environment Programme.

Reference

- Ball, W. T., Alsing, J., Staehelin, J., Davis, S. M., Froidevaux, L., and Peter, T.: Stratospheric ozone trends for 1985–2018: sensitivity to recent large variability, *Atmos. Chem. Phys.*, 19, 12731-12748, 10.5194/acp-19-12731-2019, 2019.
- 755 Boersma, K. F., Eskes, H. J., Richter, A., De Smedt, I., Lorente, A., Beirle, S., van Geffen, J. H. G. M., Zara, M., Peters, E., Van Roozendaal, M., Wagner, T., Maasakkers, J. D., van der A, R. J., Nightingale, J., De Rudder, A., Irie, H., Pinardi, G., Lambert, J. C., and Compernelle, S. C.: Improving algorithms and uncertainty estimates for satellite NO₂ retrievals: results from the quality assurance for the essential climate variables (QA4ECV) project, *Atmos. Meas. Tech.*, 11, 6651-6678, 10.5194/amt-11-6651-2018, 2018.
- 760 Belmonte Rivas, M., Veeffkind, P., Eskes, H., and Levelt, P.: OMI tropospheric NO₂ profiles from cloud slicing: constraints on surface emissions, convective transport and lightning NO₂, *Atmos. Chem. Phys.*, 15, 13519-13553, 10.5194/acp-15-13519-2015, 2015.
- Boersma, K. F., Jacob, D. J., Eskes, H. J., Pinder, R. W., Wang, J., and van der A, R. J.: Intercomparison of SCIAMACHY and OMI tropospheric NO₂ columns: Observing the diurnal evolution of chemistry and emissions from space, 113, <https://doi.org/10.1029/2007JD008816>, 2008.
- 765 Boersma, K. F., Jacob, D. J., Trainic, M., Rudich, Y., DeSmedt, I., Dirksen, R., and Eskes, H. J.: Validation of urban NO₂ concentrations and their diurnal and seasonal variations observed from the SCIAMACHY and OMI sensors using in situ surface measurements in Israeli cities, *Atmos. Chem. Phys.*, 9, 3867-3879, 10.5194/acp-9-3867-2009, 2009.
- 770 Bousquet, P., Hauglustaine, D. A., Peylin, P., Carouge, C., and Ciais, P.: Two decades of OH variability as inferred by an inversion of atmospheric transport and chemistry of methyl chloroform, *Atmos. Chem. Phys.*, 5, 2635-2656, 10.5194/acp-5-2635-2005, 2005.
- Cheng, S., Ma, J., Cheng, W., Yan, P., Zhou, H., Zhou, L., and Yang, P.: Tropospheric NO₂ vertical column densities retrieved from ground-based MAX-DOAS measurements at Shangdianzi regional atmospheric background station in China, *Journal of Environmental Sciences*, 80, 186-196, <https://doi.org/10.1016/j.jes.2018.12.012>, 2019.
- 775 Choi, S., Joiner, J., Choi, Y., Duncan, B. N., Vasilkov, A., Krotkov, N., and Bucsela, E.: First estimates of global free-tropospheric NO₂ abundances derived using a cloud-slicing technique applied to satellite observations from the Aura Ozone Monitoring Instrument (OMI), *Atmos. Chem. Phys.*, 14, 10565-10588, 10.5194/acp-14-10565-2014, 2014.
- 780 Compernelle, S., Verhoelst, T., Pinardi, G., Granville, J., Hubert, D., Keppens, A., Niemeijer, S., Rino, B., Bais, A., Beirle, S., Boersma, F., Burrows, J. P., De Smedt, I., Eskes, H., Goutail, F., Hendrick, F., Lorente, A., Pazmino, A., Piders, A., Peters, E., Pommereau, J. P., Remmers, J., Richter, A., van Geffen, J., Van Roozendaal, M., Wagner, T., and Lambert, J. C.: Validation of Aura-OMI QA4ECV NO₂ climate data
- 785

records with ground-based DOAS networks: the role of measurement and comparison uncertainties, *Atmos. Chem. Phys.*, 20, 8017-8045, 10.5194/acp-20-8017-2020, 2020.

Cooper, M. J., Martin, R. V., McLinden, C. A., and Brook, J. R.: Inferring ground-level nitrogen dioxide concentrations at fine spatial resolution applied to the TROPOMI satellite instrument, *Environmental Research Letters*, 15, 104013, 10.1088/1748-9326/aba3a5, 2020.

790 Deeter, M. N., Edwards, D. P., Francis, G. L., Gille, J. C., Martínez-Alonso, S., Worden, H. M., and Sweeney, C.: A climate-scale satellite record for carbon monoxide: the MOPITT Version 7 product, *Atmos. Meas. Tech.*, 10, 2533-2555, 10.5194/amt-10-2533-2017, 2017.

Ed Dlugokencky, NOAA/GML (gml.noaa.gov/ccgg/trends_ch4/), 2022

795 Emmerson, K. M. and Evans, M. J.: Comparison of tropospheric gas-phase chemistry schemes for use within global models, *Atmos. Chem. Phys.*, 9, 1831-1845, 10.5194/acp-9-1831-2009, 2009.

Emmons, L. K., Walters, S., Hess, P. G., Lamarque, J. F., Pfister, G. G., Fillmore, D., Granier, C., Guenther, A., Kinnison, D., Laepple, T., Orlando, J., Tie, X., Tyndall, G., Wiedinmyer, C., Baughcum, S. L., and Kloster, S.: Description and evaluation of the Model for Ozone and Related chemical Tracers, version 4 (MOZART-4), *Geosci. Model Dev.*, 3, 43-67, 10.5194/gmd-3-43-2010, 2010.

800 Forster, P., T. Storelvmo, K. Armour, W. Collins, J.-L. Dufresne, D. Frame, D.J. Lunt, T. Mauritsen, M.D. Palmer, M. Watanabe, M. Wild, and H. Zhang, 2021: The Earth's Energy Budget, Climate Feedbacks, and Climate Sensitivity. In *Climate Change 2021: The Physical Science Basis. Contribution of Working Group I to the Sixth Assessment Report of the Intergovernmental Panel on Climate Change* [Masson-Delmotte, V., P. Zhai, A. Pirani, S.L. Connors, C. Pean, S. Berger, N. Caud, Y. Chen, L. Goldfarb, M.I. Gomis, M. Huang, K. Leitzell, E. Lonnoy, J.B.R. Matthews, T.K. Maycock, T. Waterfield, O. Yelekci, R. Yu, and B. Zhou (eds.)]. Cambridge University Press, Cambridge, United Kingdom and New York, NY, USA, pp. 923–1054, 10.1017/9781009157896.009.

Frith, S. M., Kramarova, N. A., Stolarski, R. S., McPeters, R. D., Bhartia, P. K., and Labow, G. J.: Recent changes in total column ozone based on the SBUV Version 8.6 Merged Ozone Data Set, *Journal of Geophysical Research: Atmospheres*, 119, 9735-9751, 10.1002/2014jd021889, 2014.

810 Geddes, J. A. and Martin, R. V.: Global deposition of total reactive nitrogen oxides from 1996 to 2014 constrained with satellite observations of NO₂ columns, *Atmos. Chem. Phys.*, 17, 10071-10091, 10.5194/acp-17-10071-2017, 2017.

815 Gelaro, R., McCarty, W., Suárez, M. J., Todling, R., Molod, A., Takacs, L., Randles, C. A., Darmenov, A., Bosilovich, M. G., Reichle, R., Wargan, K., Coy, L., Cullather, R., Draper, C., Akella, S., Buchard, V., Conaty, A., da Silva, A. M., Gu, W., Kim, G.-K., Koster, R., Lucchesi, R., Merkova, D., Nielsen, J. E., Partyka, G., Pawson, S., Putman, W., Rienecker, M., Schubert, S. D., Sienkiewicz, M., and Zhao, B.: The Modern-Era Retrospective Analysis for Research and Applications, Version 2 (MERRA-2), *Journal of Climate*, 30, 5419-5454, 10.1175/jcli-d-16-0758.1, 2017.

820

- González Abad, G., Liu, X., Chance, K., Wang, H., Kurosu, T. P., and Suleiman, R.: Updated Smithsonian Astrophysical Observatory Ozone Monitoring Instrument (SAO OMI) formaldehyde retrieval, *Atmos. Meas. Tech.*, 8, 19-32, 10.5194/amt-8-19-2015, 2015.
- 825 Hegglin, M. I. and Lamarque, J.-F.: The IGAC/SPARC Chemistry-Climate Model Initiative Phase-1 (CCMI-1) model data output, NCAS British Atmospheric Data Centre, [ADD ACCESS DATE], available at: <http://catalogue.ceda.ac.uk/uuid/> (last access: December 2019), 2015.
- Jackson, R. B., Saunio, S., Bousquet, P., Canadell, J. G., Poulter, B., Stavert, A. R., Bergamaschi, P., Niwa, Y., Segers, A., Tsuruta, A. Increasing anthropogenic methane emissions arise equally from agricultural and fossil fuel sources. *Environmental Research Letters* 15: 071002, 2020.
- 830 Jaffe, D.: Nitrogen Cycle, Atmospheric, in: *Encyclopedia of Physical Science and Technology* (Third Edition), edited by: Meyers, R. A., Academic Press, New York, 431-440, <https://doi.org/10.1016/B0-12-227410-5/00922-4>, 2003.
- Jiang, J. H., Su, H., Zhai, C., Wu, L., Minschwaner, K., Molod, A. M., and Tompkins, A. M.: An assessment of upper troposphere and lower stratosphere water vapor in MERRA, MERRA2, and ECMWF reanalyses using Aura MLS observations, 120, 11,468-411,485, <https://doi.org/10.1002/2015JD023752>, 2015.
- 835 Kirschke, S., Bousquet, P., Ciais, P., Saunio, M., Canadell, J. G., Dlugokencky, E. J., Bergamaschi, P., Bergmann, D., Blake, D. R., Bruhwiler, L., Cameron-Smith, P., Castaldi, S., Chevallier, F., Feng, L., Fraser, A., Heimann, M., Hodson, E. L., Houweling, S., Josse, B., Fraser, P. J., Krummel, P. B., Lamarque, J.-F., Langenfelds, R. L., Le Quéré, C., Naik, V., O'Doherty, S., Palmer, P. I., Pison, I., Plummer, D., Poulter, B., Prinn, R. G., Rigby, M., Ringeval, B., Santini, M., Schmidt, M., Shindell, D. T., Simpson, I. J., Spahni, R., Steele, L. P., Strode, S. A., Sudo, K., Szopa, S., van der Werf, G. R., Voulgarakis, A., van Weele, M., Weiss, R. F., Williams, J. E., and Zeng, G.: Three decades of global methane sources and sinks, *Nature Geoscience*, 6, 813, 10.1038/ngeo1955, 2013
- 840 Krol, M. and Lelieveld, J.: Can the variability in tropospheric OH be deduced from measurements of 1,1,1-trichloroethane (methyl chloroform)?, *Journal of Geophysical Research: Atmospheres*, 108, 10.1029/2002jd002423, 2003.
- Lamarque, J. F., Emmons, L. K., Hess, P. G., Kinnison, D. E., Tilmes, S., Vitt, F., Heald, C. L., Holland, E. A., Lauritzen, P. H., Neu, J., Orlando, J. J., Rasch, P. J., and Tyndall, G. K.: CAM-chem: description and evaluation of interactive atmospheric chemistry in the Community Earth System Model, *Geosci. Model Dev.*, 5, 369-411, 10.5194/gmd-5-369-2012, 2012.
- 850 Lelieveld, J., Gromov, S., Pozzer, A., and Taraborrelli, D.: Global tropospheric hydroxyl distribution, budget and reactivity, *Atmospheric Chemistry and Physics*, 16, 12477-12493, 10.5194/acp-16-12477-2016, 2016.
- 855 Lelieveld, J., Butler, T. M., Crowley, J. N., Dillon, T. J., Fischer, H., Ganzeveld, L., Harder, H., Lawrence, M. G., Martinez, M., Taraborrelli, D., and Williams, J.: Atmospheric oxidation capacity sustained by a tropical forest, *Nature*, 452, 737-740, 10.1038/nature06870, 2008.

- Levy, H.: Normal Atmosphere: Large Radical and Formaldehyde Concentrations Predicted, *Science*, 173, 141-143, 10.1126/science.173.3992.141, 1971.
- 860 Mar, K. A., Unger, C., Waldendorff, L., and Butler, T.: Beyond CO₂ equivalence: The impacts of methane on climate, ecosystems, and health, *Environmental Science & Policy*, 134, 127-136, <https://doi.org/10.1016/j.envsci.2022.03.027>, 2022.
- Marais, E. A., Roberts, J. F., Ryan, R. G., Eskes, H., Boersma, K. F., Choi, S., Joiner, J., Abuhassan, N., Redondas, A., Grutter, M., Cede, A., Gomez, L., and Navarro-Comas, M.: New observations of NO₂ in
865 the upper troposphere from TROPOMI, *Atmos. Meas. Tech.*, 14, 2389-2408, 10.5194/amt-14-2389-2021, 2021.
- Miyazaki, K., Bowman, K., Sekiya, T., Eskes, H., Boersma, F., Worden, H., Livesey, N., Payne, V. H., Sudo, K., Kanaya, Y., Takigawa, M., and Ogochi, K.: Updated tropospheric chemistry reanalysis and emission estimates, TCR-2, for 2005–2018, *Earth Syst. Sci. Data*, 12, 2223-2259, 10.5194/essd-12-2223-
870 2020, 2020.
- Molod, A., Takacs, L., Suarez, M., Bacmeister, J., Song, I.-S., and Eichmann, A.: The GEOS Atmospheric General Circulation Model: Mean Climate and Development from MERRA to Fortuna, *NASA Technical Report Series on Global Modeling and Data Assimilation*, NASA TM-2012-104606, 28, 117 pp., 2012.
- Molod, A., Takacs, L., Suarez, M., and Bacmeister, J.: Development of the GEOS-5 atmospheric general
875 circulation model: evolution from MERRA to MERRA2, *Geosci. Model Dev.*, 8, 1339-1356, 10.5194/gmd-8-1339-2015, 2015.
- Monks, S. A., Arnold, S. R., Emmons, L. K., Law, K. S., Turquety, S., Duncan, B. N., Flemming, J., Huijnen, V., Tilmes, S., Langner, J., Mao, J., Long, Y., Thomas, J. L., Steenrod, S. D., Raut, J. C., Wilson, C., Chipperfield, M. P., Diskin, G. S., Weinheimer, A., Schlager, H., and Ancellet, G.: Multi-model study
880 of chemical and physical controls on transport of anthropogenic and biomass burning pollution to the Arctic, *Atmos. Chem. Phys.*, 15, 3575-3603, 10.5194/acp-15-3575-2015, 2015.
- Montzka, S. A., Krol, M., Dlugokencky, E., Hall, B., Jöckel, P., and Lelieveld, J.: Small Interannual Variability of Global Atmospheric Hydroxyl, *Science*, 331, 67-69, 10.1126/science.1197640, 2011.
- Morgenstern, O., Hegglin, M. I., Rozanov, E., amp, apos, Connor, F. M., Abraham, N. L., Akiyoshi, H.,
885 Archibald, A. T., Bekki, S., Butchart, N., Chipperfield, M. P., Deushi, M., Dhomse, S. S., Garcia, R. R., Hardiman, S. C., Horowitz, L. W., Jöckel, P., Josse, B., Kinnison, D., Lin, M., Mancini, E., Manyin, M. E., Marchand, M., Marécal, V., Michou, M., Oman, L. D., Pitari, G., Plummer, D. A., Revell, L. E., Saint-Martin, D., Schofield, R., Stenke, A., Stone, K., Sudo, K., Tanaka, T. Y., Tilmes, S., Yamashita, Y., Yoshida, K., and Zeng, G.: Review of the global models used within phase 1 of the Chemistry–Climate Model
890 Initiative (CCMI), *Geoscientific Model Development*, 10, 639-671, 10.5194/gmd-10-639-2017, 2017.
- Murray, L. T., Logan, J. A., and Jacob, D. J.: Interannual variability in tropical tropospheric ozone and OH: The role of lightning, *Journal of Geophysical Research: Atmospheres*, 118, 11,468-411,480, 10.1002/jgrd.50857, 2013.
- Murray, L. T., Fiore, A. M., Shindell, D. T., Naik, V., and Horowitz, L. W.: Large uncertainties in global

895 hydroxyl projections tied to fate of reactive nitrogen and carbon, 118, e2115204118,
doi:10.1073/pnas.2115204118, 2021.

Naik, V., Voulgarakis, A., Fiore, A. M., Horowitz, L. W., Lamarque, J. F., Lin, M., Prather, M. J., Young,
P. J., Bergmann, D., Cameron-Smith, P. J., Cionni, I., Collins, W. J., Dalsøren, S. B., Doherty, R., Eyring,
V., Faluvegi, G., Folberth, G. A., Josse, B., Lee, Y. H., MacKenzie, I. A., Nagashima, T., van Noije, T. P.
900 C., Plummer, D. A., Righi, M., Rumbold, S. T., Skeie, R., Shindell, D. T., Stevenson, D. S., Strode, S.,
Sudo, K., Szopa, S., and Zeng, G.: Preindustrial to present-day changes in tropospheric hydroxyl radical
and methane lifetime from the Atmospheric Chemistry and Climate Model Intercomparison Project
(ACCMIP), *Atmospheric Chemistry and Physics*, 13, 5277-5298, 10.5194/acp-13-5277-2013, 2013.

Naus, S., Montzka, S. A., Patra, P. K., and Krol, M. C.: A three-dimensional-model inversion of methyl
905 chloroform to constrain the atmospheric oxidative capacity, *Atmos. Chem. Phys.*, 21, 4809-4824,
10.5194/acp-21-4809-2021, 2021.

Naus, S., Montzka, S. A., Pandey, S., Basu, S., Dlugokencky, E. J., and Krol, M.: Constraints and biases
in a tropospheric two-box model of OH, *Atmos. Chem. Phys.*, 19, 407-424, 10.5194/acp-19-407-2019,
2019.

910 Nicely, J. M., Salawitch, R. J., Canty, T., Anderson, D. C., Arnold, S. R., Chipperfield, M. P., Emmons, L.
K., Flemming, J., Huijnen, V., Kinnison, D. E., Lamarque, J.-F., Mao, J., Monks, S. A., Steenrod, S. D.,
Tilmes, S., and Turquety, S.: Quantifying the causes of differences in tropospheric OH within global
models, *Journal of Geophysical Research: Atmospheres*, 122, 1983-2007, 10.1002/2016jd026239, 2017.

Nicely, J. M., Canty, T. P., Manyin, M., Oman, L. D., Salawitch, R. J., Steenrod, S. D., Strahan, S. E., and
915 Strode, S. A.: Changes in Global Tropospheric OH Expected as a Result of Climate Change Over the Last
Several Decades, *Journal of Geophysical Research: Atmospheres*, 123, 774-710,795,
doi:10.1029/2018JD028388, 2018.

Nicely, J. M., Duncan, B. N., Hanisco, T. F., Wolfe, G. M., Salawitch, R. J., Deushi, M., Haslerud, A. S.,
Jöckel, P., Josse, B., Kinnison, D. E., Klekociuk, A., Manyin, M. E., Marécal, V., Morgenstern, O., Murray,
920 L. T., Myhre, G., Oman, L. D., Pitari, G., Pozzer, A., Quaglia, I., Revell, L. E., Rozanov, E., Stenke, A.,
Stone, K., Strahan, S., Tilmes, S., Tost, H., Westervelt, D. M., and Zeng, G.: A machine learning
examination of hydroxyl radical differences among model simulations for CCMI-1, *Atmos. Chem. Phys.*,
20, 1341-1361, 10.5194/acp-20-1341-2020, 2020.

Nielsen, J. E., Pawson, S., Molod, A., Auer, B., da Silva, A. M., Douglass, A. R., Duncan, B., Liang, Q.,
925 Manyin, M., and Oman, L. D.: Chemical mechanisms and their applications in the Goddard Earth
Observing System (GEOS) earth system model, *Journal of advances in modeling earth systems*, 9, 3019-
3044, 2017.

Nisbet, E. G., Manning, M. R., Dlugokencky, E. J., Fisher, R. E., Lowry, D., Michel, S. E., Myhre, C. L.,
Platt, S. M., Allen, G., Bousquet, P., Brownlow, R., Cain, M., France, J. L., Hermansen, O., Hossaini, R.,
930 Jones, A. E., Levin, I., Manning, A. C., Myhre, G., Pyle, J. A., Vaughn, B., Warwick, N. J., and White, J.
W. C.: Very strong atmospheric methane growth in the four years 2014-2017: Implications for the Paris

Agreement, *Global Biogeochemical Cycles*, 33, 318–342, doi:10.1029/2018GB006009, 2019.

Oman, L. D., Douglass, A. R., Ziemke, J. R., Rodriguez, J. M., Waugh, D. W., and Nielsen, J. E.: The ozone response to ENSO in Aura satellite measurements and a chemistry-climate simulation, 118, 965-976, <https://doi.org/10.1029/2012JD018546>, 2013.

Oman, L. D., Ziemke, J. R., Douglass, A. R., Waugh, D. W., Lang, C., Rodriguez, J. M., and Nielsen, J. E.: The response of tropical tropospheric ozone to ENSO, 38, <https://doi.org/10.1029/2011GL047865>, 2011.

Patra, P. K., Krol, M. C., Prinn, R. G., Takigawa, M., Mühle, J., Montzka, S. A., Lal, S., Yamashita, Y., Naus, S., Chandra, N., Weiss, R. F., Krummel, P. B., Fraser, P. J., O'Doherty, S., and Elkins, J. W.: Methyl Chloroform Continues to Constrain the Hydroxyl (OH) Variability in the Troposphere, *Journal of Geophysical Research: Atmospheres*, 126, e2020JD033862, <https://doi.org/10.1029/2020JD033862>, 2021.

Patra, P. K., Krol, M. C., Montzka, S. A., Arnold, T., Atlas, E. L., Lintner, B. R., Stephens, B. B., Xiang, B., Elkins, J. W., Fraser, P. J., Ghosh, A., Hints, E. J., Hurst, D. F., Ishijima, K., Krummel, P. B., Miller, B. R., Miyazaki, K., Moore, F. L., Mühle, J., O'Doherty, S., Prinn, R. G., Steele, L. P., Takigawa, M., Wang, H. J., Weiss, R. F., Wofsy, S. C., and Young, D.: Observational evidence for interhemispheric hydroxyl-radical parity, *Nature*, 513, 219, [10.1038/nature13721](https://doi.org/10.1038/nature13721), 2014.

Prather, M. J., Holmes, C. D., and Hsu, J.: Reactive greenhouse gas scenarios: Systematic exploration of uncertainties and the role of atmospheric chemistry, *Geophysical Research Letters*, 39, L09803, doi:10.1029/2012GL051440, 2012.

Prinn, R. G., Huang, J., Weiss, R. F., Cunnold, D. M., Fraser, P. J., Simmonds, P. G., McCulloch, A., Harth, C., Salameh, P., O'Doherty, S., Wang, R. H. J., Porter, L., and Miller, B. R.: Evidence for Substantial Variations of Atmospheric Hydroxyl Radicals in the Past Two Decades, *Science*, 292, 1882-1888, [10.1126/science.1058673](https://doi.org/10.1126/science.1058673), 2001.

Rigby, M., Montzka, S. A., Prinn, R. G., White, J. W. C., Young, D., O'Doherty, S., Lunt, M. F., Ganesan, A. L., Manning, A. J., Simmonds, P. G., Salameh, P. K., Harth, C. M., Mühle, J., Weiss, R. F., Fraser, P. J., Steele, L. P., Krummel, P. B., McCulloch, A., and Park, S.: Role of atmospheric oxidation in recent methane growth, *Proc Natl Acad Sci U S A*, 114, 5373-5377, [10.1073/pnas.1616426114](https://doi.org/10.1073/pnas.1616426114), 2017.

Sander, S. P., Abbatt, J., Barker, J. R., Burkholder, J. B., Friedl, R. R., Golden, D. M., Huie, R., Kurylo, M. J., Moortgat, G. K., Orkin, V. L., and Wine, P. H.: Chemical kinetics and photochemical data for use in atmospheric studies evaluation number 17, Pasadena, CA: Jet Propulsion Laboratory, National Aeronautics and Space Administration, 2011, 2011.

Saunois, M., Bousquet, P., Poulter, B., Peregon, A., Ciais, P., Canadell, J. G., Dlugokencky, E. J., Etiope, G., Bastviken, D., Houweling, S., Janssens-Maenhout, G., Tubiello, F. N., Castaldi, S., Jackson, R. B., Alexe, M., Arora, V. K., Beerling, D. J., Bergamaschi, P., Blake, D. R., Brailsford, G., Bruhwiler, L., Crevoisier, C., Crill, P., Covey, K., Frankenberg, C., Gedney, N., Höglund-Isaksson, L., Ishizawa, M., Ito, A., Joos, F., Kim, H. S., Kleinen, T., Krummel, P., Lamarque, J. F., Langenfelds, R., Locatelli, R., Machida,

T., Maksyutov, S., Melton, J. R., Morino, I., Naik, V., O'Doherty, S., Parmentier, F. J. W., Patra, P. K.,
970 Peng, C., Peng, S., Peters, G. P., Pison, I., Prinn, R., Ramonet, M., Riley, W. J., Saito, M., Santini, M.,
Schroeder, R., Simpson, I. J., Spahni, R., Takizawa, A., Thornton, B. F., Tian, H., Tohjima, Y., Viovy, N.,
Voulgarakis, A., Weiss, R., Wilton, D. J., Wiltshire, A., Worthy, D., Wunch, D., Xu, X., Yoshida, Y., Zhang,
B., Zhang, Z., and Zhu, Q.: Variability and quasi-decadal changes in the methane budget over the period
2000–2012, *Atmos. Chem. Phys.*, 17, 11135–11161, 10.5194/acp-17-11135-2017, 2017.

975 Saunois, M., Bousquet, P., Poulter, B., Peregon, A., Ciais, P., Canadell, J. G., Dlugokencky, E. J., Etiope,
G., Bastviken, D., Houweling, S., Janssens-Maenhout, G., Tubiello, F. N., Castaldi, S., Jackson, R. B.,
Alexe, M., Arora, V. K., Beerling, D. J., Bergamaschi, P., Blake, D. R., Brailsford, G., Brovkin, V.,
Bruhwiler, L., Crevoisier, C., Crill, P., Covey, K., Curry, C., Frankenberg, C., Gedney, N., Höglund-
Isaksson, L., Ishizawa, M., Ito, A., Joos, F., Kim, H. S., Kleinen, T., Krummel, P., Lamarque, J. F.,
980 Langenfelds, R., Locatelli, R., Machida, T., Maksyutov, S., McDonald, K. C., Marshall, J., Melton, J. R.,
Morino, I., Naik, V., O'Doherty, S., Parmentier, F. J. W., Patra, P. K., Peng, C., Peng, S., Peters, G. P.,
Pison, I., Prigent, C., Prinn, R., Ramonet, M., Riley, W. J., Saito, M., Santini, M., Schroeder, R., Simpson,
I. J., Spahni, R., Steele, P., Takizawa, A., Thornton, B. F., Tian, H., Tohjima, Y., Viovy, N., Voulgarakis,
A., van Weele, M., van der Werf, G. R., Weiss, R., Wiedinmyer, C., Wilton, D. J., Wiltshire, A., Worthy,
985 D., Wunch, D., Xu, X., Yoshida, Y., Zhang, B., Zhang, Z., and Zhu, Q.: The global methane budget 2000–
2012, *Earth Syst. Sci. Data*, 8, 697–751, 10.5194/essd-8-697-2016, 2016.

Saunois, M., Stavert, A. R., Poulter, B., Bousquet, P., Canadell, J. G., Jackson, R. B., Raymond, P. A.,
Dlugokencky, E. J., Houweling, S., Patra, P. K., Ciais, P., Arora, V. K., Bastviken, D., Bergamaschi, P.,
Blake, D. R., Brailsford, G., Bruhwiler, L., Carlson, K. M., Carrol, M., Castaldi, S., Chandra, N.,
990 Crevoisier, C., Crill, P. M., Covey, K., Curry, C. L., Etiope, G., Frankenberg, C., Gedney, N., Hegglin, M.
I., Höglund-Isaksson, L., Hugelius, G., Ishizawa, M., Ito, A., Janssens-Maenhout, G., Jensen, K. M., Joos,
F., Kleinen, T., Krummel, P. B., Langenfelds, R. L., Laruelle, G. G., Liu, L., Machida, T., Maksyutov, S.,
McDonald, K. C., McNorton, J., Miller, P. A., Melton, J. R., Morino, I., Müller, J., Murguia-Flores, F.,
Naik, V., Niwa, Y., Noce, S., O'Doherty, S., Parker, R. J., Peng, C., Peng, S., Peters, G. P., Prigent, C.,
995 Prinn, R., Ramonet, M., Regnier, P., Riley, W. J., Rosentretter, J. A., Segers, A., Simpson, I. J., Shi, H.,
Smith, S. J., Steele, L. P., Thornton, B. F., Tian, H., Tohjima, Y., Tubiello, F. N., Tsuruta, A., Viovy, N.,
Voulgarakis, A., Weber, T. S., van Weele, M., van der Werf, G. R., Weiss, R. F., Worthy, D., Wunch, D.,
Yin, Y., Yoshida, Y., Zhang, W., Zhang, Z., Zhao, Y., Zheng, B., Zhu, Q., Zhu, Q., and Zhuang, Q.: The
Global Methane Budget 2000–2017, *Earth Syst. Sci. Data*, 12, 1561–1623, 10.5194/essd-12-1561-2020,
1000 2020.

Spivakovsky, C. M., Logan, J. A., Montzka, S. A., Balkanski, Y. J., Foreman-Fowler, M., Jones, D. B. A.,
Horowitz, L. W., Fusco, A. C., Brenninkmeijer, C. A. M., Prather, M. J., Wofsy, S. C., and McElroy, M.
B.: Three-dimensional climatological distribution of tropospheric OH: Update and evaluation, *Journal of
Geophysical Research: Atmospheres*, 105, 8931–8980, 10.1029/1999jd901006, 2000.

1005 Strode, S. A., Duncan, B. N., Yegorova, E. A., Kouatchou, J., Ziemke, J. R., and Douglass, A. R.:

Implications of carbon monoxide bias for methane lifetime and atmospheric composition in chemistry climate models, *Atmos. Chem. Phys.*, 15, 11789-11805, 10.5194/acp-15-11789-2015, 2015.

Tilmes, S., Lamarque, J. F., Emmons, L. K., Kinnison, D. E., Marsh, D., Garcia, R. R., Smith, A. K., Neely, R. R., Conley, A., Vitt, F., Val Martin, M., Tanimoto, H., Simpson, I., Blake, D. R., and Blake, N.: Representation of the Community Earth System Model (CESM1) CAM4-chem within the Chemistry-Climate Model Initiative (CCMI), *Geosci. Model Dev.*, 9, 1853-1890, 10.5194/gmd-9-1853-2016, 2016.

1010 Tilmes, S., Lamarque, J. F., Emmons, L. K., Kinnison, D. E., Ma, P. L., Liu, X., Ghan, S., Bardeen, C., Arnold, S., Deeter, M., Vitt, F., Ryerson, T., Elkins, J. W., Moore, F., Spackman, J. R., and Val Martin, M.: Description and evaluation of tropospheric chemistry and aerosols in the Community Earth System Model (CESM1.2), *Geosci. Model Dev.*, 8, 1395-1426, 10.5194/gmd-8-1395-2015, 2015.

1015 Turner, A. J., Frankenberg, C., Wennberg, P. O., and Jacob, D. J.: Ambiguity in the causes for decadal trends in atmospheric methane and hydroxyl, *Proc Natl Acad Sci U S A*, 114, 5367-5372, 10.1073/pnas.1616020114, 2017.

Turner, A. J., Fung, I., Naik, V., Horowitz, L. W., and Cohen, R. C.: Modulation of hydroxyl variability by ENSO in the absence of external forcing, *Proceedings of the National Academy of Sciences*, 115, 8931-8936, 10.1073/pnas.1807532115, 2018.

1020 Young, P. J., Naik, V., Fiore, A. M., Gaudel, A., Guo, J., Lin, M. Y., Neu, J. L., Parrish, D. D., Rieder, H. E., Schnell, J. L., Tilmes, S., Wild, O., Zhang, L., Ziemke, J. R., Brandt, J., Delcloo, A., Doherty, R. M., Geels, C., Hegglin, M. I., Hu, L., Im, U., Kumar, R., Luhar, A., Murray, L., Plummer, D., Rodriguez, J., Saiz-Lopez, A., Schultz, M. G., Woodhouse, M. T., and Zeng, G.: Tropospheric Ozone Assessment Report: Assessment of global-scale model performance for global and regional ozone distributions, variability, and trends, *Elementa*, 6, 10, <https://doi.org/10.1525/elementa.265>, 2018.

1025 Zhang, Y., Cooper, O. R., Gaudel, A., Thompson, A. M., Nédélec, P., Ogino, S.-Y., and West, J. J.: Tropospheric ozone change from 1980 to 2010 dominated by equatorward redistribution of emissions, *Nature Geoscience*, 9, 875-879, 10.1038/ngeo2827, 2016.

1030 Zhao, Y., Saunio, M., Bousquet, P., Lin, X., Berchet, A., Hegglin, M. I., Canadell, J. G., Jackson, R. B., Dlugokencky, E. J., Langenfelds, R. L., Ramonet, M., Worthy, D., and Zheng, B.: Influences of hydroxyl radicals (OH) on top-down estimates of the global and regional methane budgets, *Atmos. Chem. Phys.*, 20, 9525-9546, 10.5194/acp-20-9525-2020, 2020a.

1035 Zhao, Y., Saunio, M., Bousquet, P., Lin, X., Berchet, A., Hegglin, M. I., Canadell, J. G., Jackson, R. B., Deushi, M., Jöckel, P., Kinnison, D., Kirner, O., Strode, S., Tilmes, S., Dlugokencky, E. J., and Zheng, B.: On the role of trend and variability in the hydroxyl radical (OH) in the global methane budget, *Atmos. Chem. Phys.*, 20, 13011-13022, 10.5194/acp-20-13011-2020, 2020b.

1040 Zhao, Y., Saunio, M., Bousquet, P., Lin, X., Berchet, A., Hegglin, M. I., Canadell, J. G., Jackson, R. B., Hauglustaine, D. A., Szopa, S., Stavert, A. R., Abraham, N. L., Archibald, A. T., Bekki, S., Deushi, M., Jöckel, P., Josse, B., Kinnison, D., Kirner, O., Marécal, V., O'Connor, F. M., Plummer, D. A., Revell, L. E., Rozanov, E., Stenke, A., Strode, S., Tilmes, S., Dlugokencky, E. J., and Zheng, B.: Inter-model

comparison of global hydroxyl radical (OH) distributions and their impact on atmospheric methane over the 2000–2016 period, *Atmos. Chem. Phys.*, 19, 13701-13723, 10.5194/acp-19-13701-2019, 2019.

1045 Zheng, B., Chevallier, F., Yin, Y., Ciais, P., Fortems-Cheiney, A., Deeter, M. N., Parker, R. J., Wang, Y., Worden, H. M., and Zhao, Y.: Global atmospheric carbon monoxide budget 2000–2017 inferred from multi-species atmospheric inversions, *Earth Syst. Sci. Data*, 11, 1411-1436, 10.5194/essd-11-1411-2019, 2019.

1050 Ziemke, J. R., Chandra, S., Duncan, B. N., Froidevaux, L., Bhartia, P. K., Levelt, P. F., and Waters, J. W.: Tropospheric ozone determined from Aura OMI and MLS: Evaluation of measurements and comparison with the Global Modeling Initiative's Chemical Transport Model, 111, <https://doi.org/10.1029/2006JD007089>, 2006.

1055

1060

1065

1070

1075

Table 1. The DSMACC model experiments.

| Species | Simulations | Description |
|---------------------------------|-------------|---|
| Ref | Ref_model | Chemical species and meteorological conditions from 3D model simulations for 2010. |
| All | All_obs | All the chemical species and meteorological conditions listed below adjusted to match observations. |
| NO ₂ | NO2_obs_PBL | Adjust boundary layer NO ₂ to match the OMI QA4ECV product. |
| O ₃ | O3_obs | Adjust tropospheric O ₃ to match OMI/MLS product. |
| CH ₄ | CH4_obs | Adjust tropospheric CH ₄ to match the assimilated data. |
| CO | CO_obs | Adjust tropospheric CO to match the assimilated data. |
| CH ₂ O | CH2O_obs | Adjust tropospheric CH ₂ O to match the assimilated data. |
| O ₃ column | O3col_obs | Adjust total ozone column to match SBUV/MOD data. |
| H ₂ O _(g) | H2O_obs | Adjust water vapor to MERRA-2 data. |
| Ta | Ta_obs | Adjust air temperatures to MERRA-2 data. |

Table 2. Modeled and observation-based estimates of global [OH]_{trop-M}, CH₄ sink by tropospheric OH (L_{CH_4+OH}) averaged during 2000-2009, and the CH₄ lifetime against tropospheric OH (τ_{CH_4+OH}).

| | | [OH] _{trop-M} (10 ⁵ molec cm ⁻³) | L_{CH_4+OH} (Tg yr ⁻¹) | τ_{CH_4+OH} (yr) |
|-------------------|----------------|---|---|--------------------------|
| Modeled | CESM1-CAM4chem | 11.9 | 540 | 9.1 |
| | GEOSCCM | 12.6 | 565 | 8.7 |
| Observation-based | CESM1-CAM4chem | 9.9 | 434 | 11.4 |
| | GEOSCCM | 10.4 | 461 | 10.7 |

Table 3. The modeled and observation-based [OH]_{trop-M} (in 10⁵molec cm⁻³) averaged over latitudinal bands during 2000-2009. The corresponding tropospheric CH₄ sink by OH (L_{CH_4+OH}) (in Tg yr⁻¹) is given in brackets.

| | | 90°-30°S | 30°S-0° | 0°-30°N | 30°-90°N |
|-------------------|----------------|----------|-----------|-----------|----------|
| Modeled | CESM1-CAM4chem | 5.9(49) | 14.2(173) | 17.8(226) | 9.4(93) |
| | GEOSCCM | 6.2(50) | 16.1(192) | 18.5(229) | 9.6(94) |
| Observation-based | CESM1-CAM4chem | 5.3(42) | 12.2(144) | 14.5(178) | 7.2(69) |
| | GEOSCCM | 5.6(46) | 13.6(161) | 14.9(183) | 7.4(72) |

Table 4. Contributions from individual factors to the difference in global $[\text{OH}]_{\text{trop-M}}$ and tropospheric CH_4 sink by reaction with OH between CESM1-CAM4chem simulated and the corresponding observation-based OH fields (modeled – observation-based).

| | $[\text{OH}]_{\text{trop-M}}$ ($10^5 \text{ molec cm}^{-3}$) | CH_4 sink (Tg yr^{-1}) |
|-----------------------------------|---|---|
| $\text{H}_2\text{O}_{(\text{g})}$ | 0.1 | 10 |
| T_a | 0 | 0 |
| Column O_3 | 0.4 | 22 |
| CO | 1.3 | 60 |
| O_3 | -0.3 | -17 |
| NO_2 | 0.3 | 22 |
| CH_4 | 0.1 | 5 |
| CH_2O | 0.1 | 6 |
| Total | 2.0 | 108 |

1095

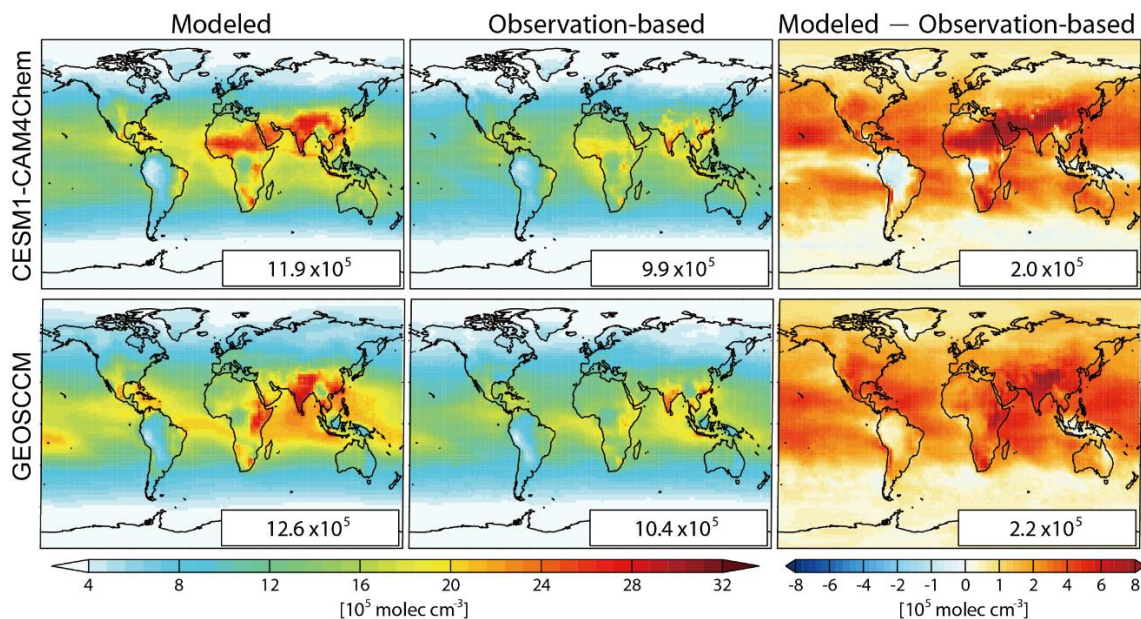


Figure 1. Spatial distributions of air mass-weighted tropospheric mean $[\text{OH}]$ ($[\text{OH}]_{\text{trop-M}}$) in 2010 from model simulations (left) and constrained by observations (middle), and the difference between modeled and observation-based $[\text{OH}]_{\text{trop-M}}$ (right) estimated from CESM1-CAM4Chem (top) and GEOSCCM (bottom) simulations. The global mean values are shown inset in molec cm^{-3} .

1100

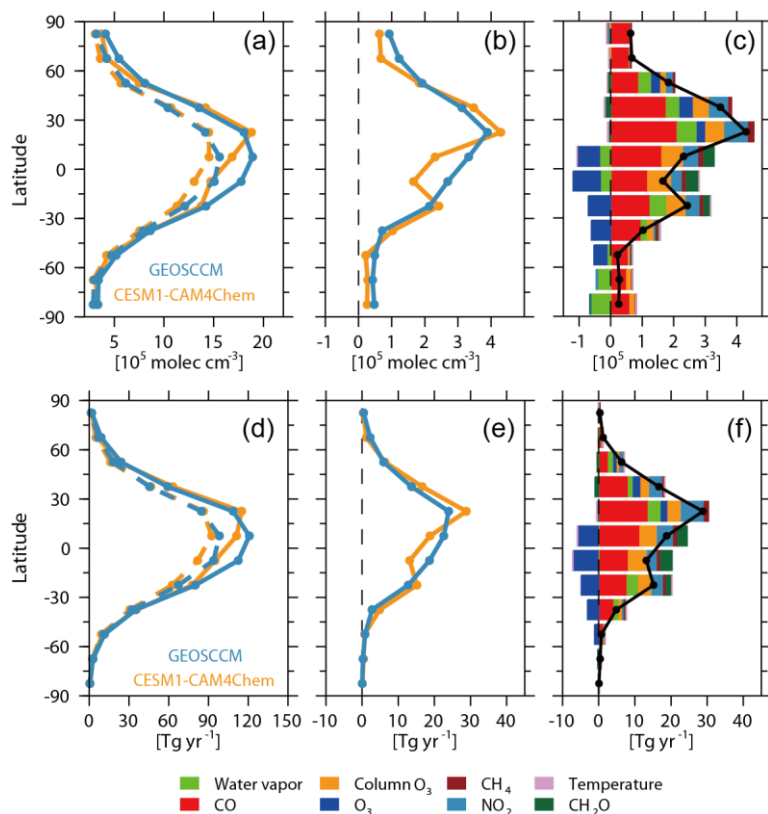
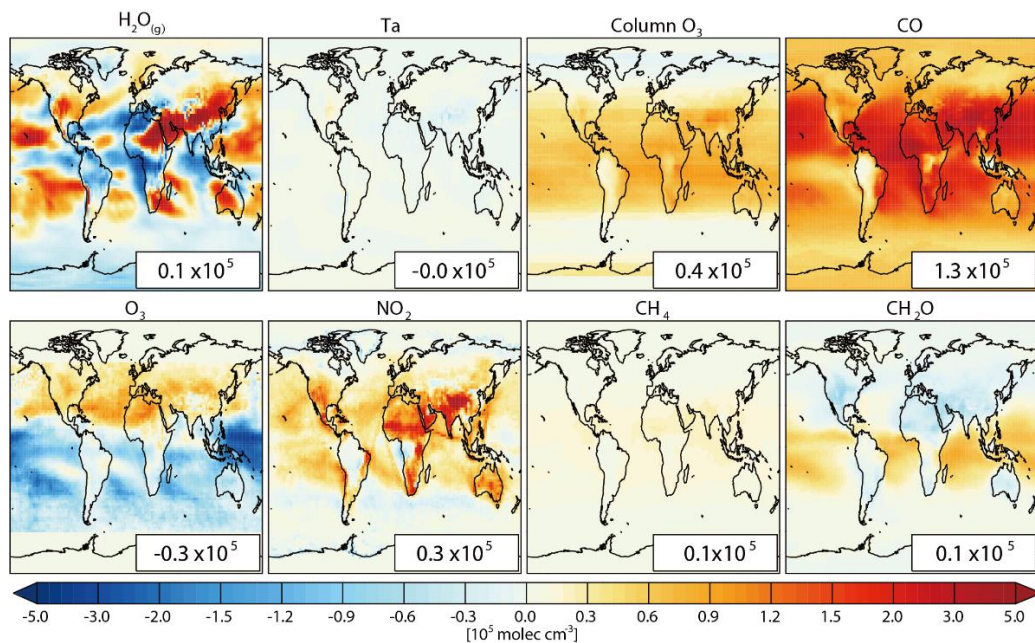
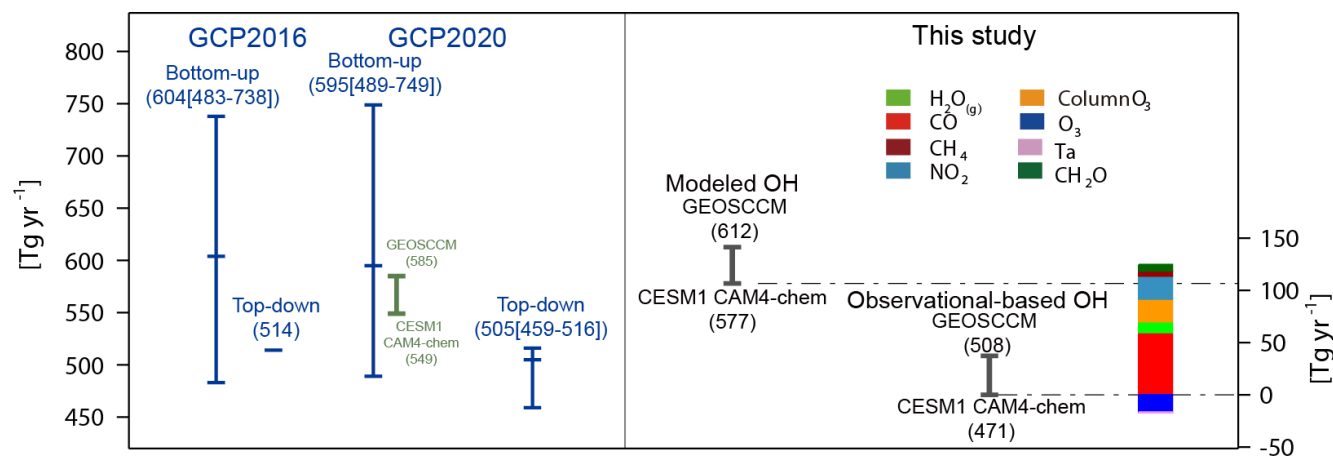


Figure 2. (a) Zonal averaged $[\text{OH}]_{\text{trop-M}}$ of modeled (solid lines) and observation-based OH field (dashes lines) estimated from CESM1 CAM4-chem (yellow) and GEOSCCM (blue) simulations. (b) Difference of zonal averaged $[\text{OH}]_{\text{trop-M}}$ between modeled and observation-based OH fields. (c) Difference between CESM1 CAM4-chem simulated and observational-based zonal averaged $[\text{OH}]_{\text{trop-M}}$ (black line) and the contribution from each OH precursor (colored bars) for zonal averaged difference. (d-f) Same as (a-c) but for the tropospheric CH_4 sink by reaction with OH.



1110

Figure 3. Spatial distributions of the contribution of individual factors to the difference between CESM1 CAM4-chem simulated and observation-based (modeled – observation-based) $[OH]_{\text{trop-M}}$. The global mean values are shown inset in molec cm^{-3} .



1115

Figure 4. Global total chemical loss of CH_4 estimated by the bottom-up and top-down methods from previous GCP global CH_4 budget (blue bars; Saunois et al., 2016; 2020), simulated by GEOSCCM and CESM1 CAM4-Chem which is included in the bottom-up estimates in Saunois et al. (2020) (green bar), and that estimated in this study using the model simulated and observation-based OH fields and assimilated surface observations of CH_4 (black bars). The colored bar shows the contribution of individual

1120

factors to the difference in the chemical loss of CH₄ between CESM1 CAM4-Chem simulated and the corresponding observation-based OH. The blue, green, and black bars are corresponding to the left axis and the colored bar is corresponding to the right axis.

1125